

# MECHANICAL BEHAVIOR OF BULK ULTRAFINE-GRAINED AND NANOCRYSTALLINE Zn

X. Zhang<sup>1</sup>, H. Wang<sup>1</sup> and C. C. Koch<sup>2</sup>

<sup>1</sup> Materials Science and Technology Division, Mail Stop G755, Los Alamos National Laboratory, Los Alamos, NM 87545, USA

<sup>2</sup> North Carolina State University, Department of Materials Science and Engineering, Raleigh, NC, 27695-7907, USA

Received: February 15, 2004

**Abstract.** Mechanical properties of bulk ultrafine-grained and nanocrystalline Zn produced by mechanical milling are reviewed. Dynamic recrystallization plays an important role in the microstructural evolution of cryomilled Zn during early milling times. The modulated oscillation of hardness during cryomilling is a combinational effect of dynamic recrystallization, average grain size, grain size distribution and dislocation density variations. Bulk ultrafine-grained and nanocrystalline Zn, synthesized by *in situ* consolidation during milling, possess high tensile ductility. Deformation mechanisms in larger grains (submicron) are different from that in nanoscale grains. Microstructure, ductility and deformation mechanisms in Zn and other ultrafine-grained and nanocrystalline elemental metals are compared. These comparisons indicate that the ductility of ultrafine-grained and nanocrystalline materials may be enhanced by the following ways (i) increasing strain hardening (ii) increasing strain rate sensitivity (iii) activating other deformation mechanisms such as twinning or stacking faults (iv) accommodating grain boundary sliding to postpone the generation of pores along the grain boundaries or triple junctions. The engineering design of materials with high strength and high tensile ductility can be achieved by optimizing the microstructures of ultrafine-grained and nanocrystalline materials.

## Table of Contents

1. Introduction	54	3.2. Lattice strain and stored enthalpy	63
2. Background	54	4. Mechanical behavior of cryomilled bulk nc Zn	67
2.1. Evolution of microstructure during mechanical milling	54	4.1. Effect of dynamic recrystallization on the mechanical behavior of compacted bulk CM Zn	67
2.1.1. Nanocrystallite formation mechanisms	54	4.2. Ductility of compacted bulk CM Zn	70
2.1.2. Evolution of grain size	55	5. The synthesis of bulk nc Zn by <i>in situ</i> consolidation of powders	72
2.1.3. Lattice strain and stored enthalpy	56	6. Mechanical properties of <i>in situ</i> consolidated bulk nc Zn	74
2.1.4. Recovery and recrystallization	56	6.1. Strength and ductility of nc Zn studied by microhardness and MDBT tests	77
2.2. Techniques that can synthesize bulk ufg and nc materials	57	6.2. Ductility and deformation mechanisms of BM Zn studied by uniaxial tensile tests	74
2.3. Deformation mechanisms	58	7. Comparisons of the microstructure and mechanical properties of bulk nc Zn prepared by cryomilling and room temperature milling	81
2.3.1. Size effect on plasticity	58		
2.3.2. Ductility	59		
3. Microstructure evolution in cryomilled Zn	60		
3.1. Nanocrystallite formation by dynamic recrystallization	60		

Corresponding author: X. Zhang, email: zhangx@lanl.gov

7.1. Grain size and its distributions as a function of temperature	81
7.2. Mechanical properties	82
7.3. Optimizing mechanical properties of bulk nc Zn by combination of the two techniques	82
8. Comparisons of deformation mechanisms in bulk ufg and nc elemental metals	84
9. Summary	90

## 1. INTRODUCTION

Recently there has been a great deal of interest in studying the mechanical behavior of bulk ultrafine-grained (ufg, grain size in the range of 100 nm – 1000nm) and nanocrystalline (nc, grain size in the range of less than 100 nm) metals and alloys. The driving forces behind these studies come from the hope that ufg and nc materials may possess both enhanced strength and ductility. The knowledge of deformation mechanisms of ufg and nc materials is critical for engineering design of these materials with high strength and high ductility. Such information can be obtained from rigorous tensile testing techniques, such as uniaxial tensile tests, by using large enough bulk specimens. There have been many techniques that can synthesize nc materials in the form of powders or thin films, eg. inert gas condensation [1], rapid solidification [2], electrodeposition [3], crystallization of amorphous phases by annealing [4], chemical processing [5], sputtering [6] and pulsed laser deposition [7]. Mechanical attrition-the ball milling of single or multicomponent powders- has also been widely used to synthesize nanostructured materials [8]. However, the techniques that can synthesize fully dense bulk nc materials are very limited. Consolidation of powders with nanoscale grain size is one of the most commonly used techniques. Porosity on the nm or  $\mu\text{m}$  level usually remains after compaction and proves to be detrimental to the ductility of nc materials. The difficulty of obtaining porosity-free bulk nc materials has stimulated extensive research on improving existing processing techniques as well as exploring new approaches, such as equal channel angular pressing [9,10], cold rolling [11], electrodeposition [12-14] and stacking of multilayers by magnetron sputtering [15]. Details on some of these techniques will be given in Section 2.2. In addition, Section 2 provides background information that may put the work of the paper in context. This section explains important basic concepts and summarizes up-to-date progress and challenges in close relevance to the article. The following subjects will be reviewed in section 2:

(1) evolution of microstructure during mechanical milling;

(2) techniques that can synthesize bulk ufg and nc materials; and  
 (3) deformation mechanisms.

In this article, we will review the microstructural evolution and mechanical properties of porosity free bulk ufg and nc Zn synthesized via several approaches: (i) cryomilling (mechanical milling performed at 77K) followed by powder compaction, (ii) *in situ* consolidation of powders during room-temperature mechanical milling (iii) a combination of cryomilling and *in situ* consolidation technique. More specifically, the article will focus on the following subjects:

- (1) evolution of microstructure (grain size and its distribution) in cryomilled (CM) Zn with emphasis on the dynamic recrystallization (DRX) phenomenon and the correlation of stored enthalpy and microstrain induced during milling (Sec. 3);
- (2) effects of DRX, grain size distribution and dislocation density variations on the mechanical properties of compacted CM Zn powders (Sec. 4);
- (3) synthesizing bulk ufg and nc Zn by *in situ* consolidation of nc Zn powders during mechanical milling at room temperature (BM) (Sec. 5);
- (4) mechanical properties and deformation mechanisms of *in situ* consolidated bulk nc Zn studied by tensile tests (Sec. 6);
- (5) comparisons of the microstructure and mechanical properties of bulk ufg and nc Zn prepared by cryomilling and room temperature ball milling (Sec. 7);
- (6) comparisons of deformation mechanisms in ufg and nc Zn with other metals and strategies to improve ductility of ufg and nc metals (Sec. 8).

Zn with ufg or nc structures will serve as the model material to illustrate basic concepts, understand the plastic deformation mechanisms and explore the possibilities of optimizing strength and ductility in ufg and nc metals from a broader point of view.

## 2. BACKGROUND

### 2.1. Evolution of microstructure during mechanical milling

#### 2.1.1. Nanocrystallite formation mechanisms

During mechanical milling, materials will often experience heavy cyclic deformation. It is believed that mechanical milling produces its nanostructures by the structural decomposition of coarser-grained (cg) structures as the result of severe plastic deformation. The current understanding of the development of nc microstructures in single-phase materials by

mechanical milling has been reviewed before [8,16]. Initial information in this regard comes from transmission electron microscopy (TEM) studies of ball-milled Ru and AlRu microstructures as a function of milling time [17,18]. These early studies propose the formation of subgrains followed by their rotation such that small nc grains possessing high angle grain boundaries are created [16]. This mechanism works reasonably well for many single-phase metals milled at room temperature. A common feature indicated by this mechanism is that nc grains with high angle grain boundaries, on the order of 10 nm or less, will be produced after a long period of milling time. However, this may not be the only operating mechanism when milling is carried out under liquid nitrogen temperature (77K), cryomilling. Dynamic recrystallization has been proposed to explain the formation of nc Zn and other materials during early stages of cryomilling or cold working [17-19]. Details on the new mechanisms for the formation of nc Zn during cryomilling will be presented in Sec. 3.2.

### 2.1.2. Evolution of grain size

Using X-ray line broadening to measure average grain size it is commonly observed that the average grain size decreases with milling time. The minimum average grain size ( $d_{min}$ ) obtainable by milling has been attributed to a balance between the defect/dislocation structure introduced by the plastic deformation of milling and its recovery by thermal processes [20]. It was also found that  $d_{min}$  scales inversely with melting temperature for selected face centered cubic (fcc) metals as shown in Fig. 1 [21] (data taken from [20, 22-26]). However, the  $d_{min}$  for body centered cubic (bcc) and hexagonal close packed (hcp) metals, and for fcc metals with higher melting temperatures, exhibit essentially constant values with melting temperature. The value of  $d_{min}$  is about 14 nm for hcp metals, 8 nm for bcc metals and 6nm for high melting point fcc metals. It had been proposed for pure metals that the limiting grain size is determined by the minimum grain size that can sustain a dislocation pile-up within a grain and by the rate of recovery [20]. It was shown that there was an approximate linear relationship between the final grain diameter and the critical equilibrium distance between two edge dislocations in a pile-up,  $L_c$ . The latter distance was calculated from the expression [27]:

$$L_c = \frac{3Gb}{\pi(1-\nu)h}, \quad (1)$$

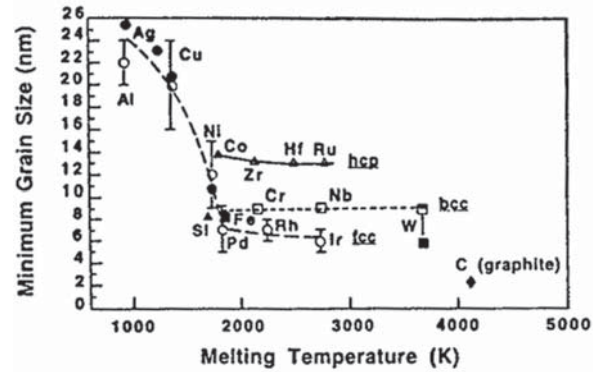


Fig. 1. Minimum grain size for nc elements vs. their melting temperatures (open symbols (20, 22); filled circles (26); Si (23, 24); C (25)).

where  $G$  is the shear modulus,  $b$  is the magnitude of the Burgers vector,  $\nu$  is Poisson's ratio,  $h$  is hardness of the material. Therefore hardening results in reduced values for  $L_c$ .

There are several factors that can influence the value of  $d_{min}$  attained by ball milling. These include the energy of mill [28], ball to powder ratio (BPR) [29], solid solution hardening [30] and milling temperature [28]. Typically, higher mill energy, larger BPR values and lower processing temperature will lead to a finer grain size. It should be noted, however, that in certain cases grain size was found to increase to a certain extent during ball milling and then decreased for further milling instead of decreasing continuously with increasing milling time [31,32]. Most previous studies focus on the evolution of average grain size during milling. Recently attention has been paid to the evolution of grain size distribution as this parameter is important for understanding mechanical behavior of nc materials [17,33,34].

### 2.1.3. Lattice strain and stored enthalpy

Studies on lattice strain and stored enthalpy will provide additional information on nc formation mechanisms. Lattice strain is usually introduced into the materials due to severe plastic deformation during milling. The effects of lattice strain and grain sizes can be separated from each other by careful analysis of the X-ray peak shapes [35,36]. The lattice strain results from the literature were summarized and plotted vs. reciprocal grain size ( $1/d$ ) by Koch [21]. Interestingly, in his plot of lattice strain vs.  $1/d$ , it has been found that for some systems, Ti [37], Pd [20], the lattice strain increased continuously with decreasing grain size and reached a maximum value at the smallest grain size. For some other

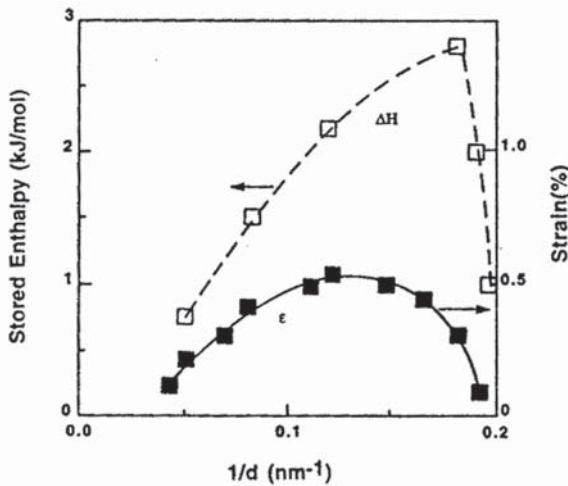


**Fig. 2.** Stored enthalpy and lattice strain vs. reciprocal grain size for W [26].

systems such as Ru [22], Al, Ni, Fe and W [26], however, the lattice strain first increases, reaches a maximum and then decreases, i.e., there is also a maximum in lattice strain with the decreasing grain size. An example of the plot of strain vs.  $1/d$  for W (solid points) is given in Fig. 2. The stored enthalpy (or stored energy) in W, represented by open data points in the same plot, followed the same trend compared with that of lattice strain. To explain the maxima in stored enthalpy with  $1/d$ , some suggested that the stored enthalpy comes mainly from grain boundaries and grain boundary strains [26]. Stress relaxation or recover may be responsible for the maxima [26]. However, the fact that the two maxima do not occur at the same grain size raises some concern for this explanation. Maxima of lattice strain and stored enthalpy were also observed in cryomilled nc Zn. Details on these results are presented in Sec. 3.2.

#### 2.1.4. Recovery and recrystallization

**Recovery.** As mentioned in Sec. 2.1.2. and 2.1.3., recovery is related to the  $d_{\min}$  obtainable during the milling process and the maxima of lattice strain in certain systems. Recovery refers to changes in the properties of deformed materials which occur prior to recrystallization; these changes are such as to partially restore the properties to their values before deformation [38]. Recovery can occur in plastically deformed materials and in crystals that possess a high density of defects, point defects and/or line defects, and reduce the defect density or strain as a result. The recovery process can be described in

several steps: the formation of dislocation cell walls in highly dislocated materials, annihilation of dislocations within the cells, the formation of subgrains and subgrain growth by either subgrain boundary migration or subgrain rotation and coalescence [38]. Complete recovery occurs when polycrystalline metals have been lightly deformed [39]. If the crystals are heavily deformed to a certain extent, however, recrystallization usually occurs [40]. As the recovery process usually happens at higher annealing temperatures, one can depress recovery by reducing the deformation temperature.

**Recrystallization.** Recovery is a relatively homogeneous process that progresses gradually without identifiable beginning or end of the process. Whereas recrystallization involves the formation of new grains, free from strains, in certain parts of the specimen and the subsequent growth of these grains to consume the deformed or recovered microstructure [38]. Both processes are driven by and consequently consume the stored energy in the deformed materials. Recovery, if it occurs first, could consume a large fraction of stored energy and therefore suppress the occurrence of recrystallization and vice versa. Recrystallization will prevail over recovery during a high strain rate, low temperature deformation process [38,41]. Mechanical milling can create very high strain and strain rate in the ball milled materials compared to that from the traditional cold rolling method, and thus create inhomogeneously distributed dislocations and defects where some regions may have a high dislocation density. These highly disordered areas may store enough energy to induce or facilitate a recrystallization process.

**Dynamic recrystallization.** Recrystallization can be categorized by comparing the sequence of recrystallization with the plastic deformation. In many cases, recrystallization occurs during post-deformation annealing processes, which is called static recrystallization. If the recrystallization occurs during deformation, however, it is called dynamic recrystallization (DRX). The nucleation mechanisms for static recrystallization include strain induced grain boundary migration [38,42] and preexisting nuclei such as dislocation cells or subgrains [43,44]. During DRX, nucleation as well as growth (grain boundary migration) takes place while the strain is being applied [45]. New grains originate at the old grain boundaries. As the materials continues to deform, the dislocation density of the new grains increases, thus reducing the driving force for further grain growth, and the recrystallized grains eventually cease to grow [40].

The nucleation mechanism for DRX is assumed to be similar to that for static recrystallization, strain induced grain boundary migration. Bulging of grain boundaries is frequently observed as a prelude to DRX. The critical nucleus diameter,  $x_c$ , for DRX is given by

$$x_c = \frac{MLGb^3\rho_m^2}{\dot{\epsilon}}, \quad (2)$$

where  $M$  is the grain boundary mobility,  $L$  is the mean slip distance of the dislocations,  $G$  is shear modulus,  $b$  is Burger vector,  $\rho_m$  is the dislocation density,  $\dot{\epsilon}$  is the strain rate. Details on derivation for this formula can be found in references 38, 46 and 47.

Under the assumption that nucleation occurs by a bulge mechanism, then the condition for the formation of a critical nucleus with diameter  $x_c$ , is

$$E > \frac{2\gamma_b}{x_c}, \quad (3)$$

where  $E$  is the stored energy and  $\gamma_b$  is the specific boundary energy.  $E$  is given by  $E = K\rho_m Gb^2$ ,  $K$  is a constant. Hence the condition for nucleation is

$$\frac{\rho_m^3}{\dot{\epsilon}} > \frac{2\gamma_b}{KMLG^2b^5}. \quad (4)$$

The terms on the right hand side are approximately constant at a particular temperature. Thus the condition for the nucleation of DRX is that a critical value of  $\rho_m/\dot{\epsilon}$  must be achieved. In materials with low stacking fault energy, recovery is slow and the dislocation density could be increased to the critical value necessary for DRX to occur. Decreasing the deformation temperature can also suppress the dislocation recovery and therefore facilitate DRX.

Different types of DRX have been identified according to their characteristics during the process. In the case of geometric DRX, grain boundaries develop serrations during dynamic recovery, and the wavelength of these serrations is similar to the subgrain size [48-50]. Although a large number of the boundaries are usually low angle grain boundaries, the fraction of high angle grain boundaries will increase with increasing strain [48]. Geometric DRX often occurs in a variety of higher stacking fault energy alloys where pronounced dynamic recovery occurs [45]. In other cases, DRX is characterized by progressive lattice rotation. New grains with high angle boundaries may be formed by the progressive rotation of subgrains with little accompanying grain boundary migration [51]. The mechanism by

which this progressive subgrain rotation occurs is not very clear. It is possible that grain boundary sliding is also involved in this process. DRX has been identified in CM Zn and is believed to be responsible for the formation of nanoscale grains with high angle grain boundaries during the early stages of cryomilling [17]. Details of DRX phenomenon in cryomilled Zn will be presented in Sec. 3.1. This phenomenon will be revisited when discussing the evolution of mechanical behavior of CM nc Zn in Sec. 4.

## 2. 2. Techniques that can synthesize bulk ufg and nc materials

Bulk ufg and nc materials can be synthesized via a two-step processing technique, production of powders with nc grains followed by compaction to achieve full density in the materials, for example the synthesis of bulk nc Cu, Pd [52] by combinations of inert gas condensation and compaction. The two-step techniques have the advantage of obtaining nc metals with a wide range of grain sizes varying from submicron to ~ 10 nm in a wide variety of materials. However, the compacted materials may not reach full density. A certain amount of controversial research, such as negative Hall-Petch relations (where below certain grain size, the hardness of materials decreases with decreasing grain size) and extremely limited tensile ductility could be related to the residual porosity in these compacted nc materials [53]. Some attempts have been made to increase the density of compacted materials. An improvement in ductility of compacted materials has been achieved [52,54].

Compared with the above-mentioned two-step processing techniques, several one-step processing techniques have been developed.

- (1) Severe plastic deformation (SPD). SPD has been shown to be an effective way to produce bulk ufg and nc materials. Details have been reviewed by Valiev *et al.* [55]. Typical SPD techniques include high pressure torsion (HPT), equal channel angular pressing (ECAP) and repetitive corrugation and straightening (RCS). These techniques produce nc or ufg by severely deforming bulk materials. Therefore as-prepared materials typically have the same density as raw materials, avoiding the generation of porosity.
- (2) Electrodeposition. Electrodeposition has been successfully used to produce bulk ufg and nc metals, such as Cu [56], Ni [57], Zn [13] and Co [14]. This technique provides several advantages: (i) synthesizing artifact-free bulk materials (ii) easy to control grain sizes from 10 nm to sub-

micron (iii) usually narrow grain size distribution. Special attention should be paid to the incorporation of certain impurities (S, O and H, *etc.*) into the materials, as some of these elements may embrittle the materials.

- (3) Flux melting and casting. Recently Shen and Schwarz successfully synthesized bulk Cu/Ag nc alloys via flux melting techniques [58,59]. First, they synthesize alloys by mechanical alloying. Then melt the alloyed powders in fused silica tube and purify the melt with a flux. By quenching the molten alloys, bulk nc metals or even amorphous alloys can be synthesized. They demonstrate that the microstructure, such as grain size, can be controlled by carefully purifying the melt with flux and choosing appropriate quenching rate [59]. Bulk nc Cu/Ag eutectic alloys synthesized via this technique possess high strength and low resistivity, making it an attractive candidate as strong structural materials for high magnetic field applications. He *et al.* [60] use casting method to obtain a nanocomposite where dendrites of a ductile Ti-rich solution were formed *in situ* within nc matrix. These nanocomposites have high strength and potentially good ductility.
- (4) Synthesizing sheet metals by roll-bonding and sputtering. Roll-bonding process has been used to synthesize bulk nc composites by cyclic rolling and stacking dissimilar metals [61]. To achieve good bonding between adjacent materials, careful surface cleaning and a high degree of deformation (50% rolling) are usually required [62]. Composites with nc grain size and in certain cases amorphous alloys can be attained [62, 63]. Misra *et al.* [15, 64] have recently performed systematic studies on Cu based multilayer films synthesized via magnetron sputtering techniques. The unique feature of this technique is that the individual layer thickness of multilayer composites can be controlled, varying from a few nm to sub-micron, while keeping the total thickness in tens or even hundreds of micron range. These bulk nc composites have unusually high strength [15] and considerable ductility as evidenced by rolling and tensile tests [64,65].

One-step processing techniques have the advantage of obtaining porosity-free bulk ufg or nc materials. The ductility of thus-prepared materials is usually higher than those prepared via two-step processing techniques. Some of these techniques have potential to mass-produce bulk ufg and nc materials and therefore stimulate the hope of commercializing bulk ufg and nc materials.

## 2. 3. Deformation mechanisms

Current understanding of the deformation mechanisms of nanostructured materials is very limited partially due to the porosity in compacted materials. Another major barrier is that it is usually difficult to produce specimens large enough for decisive tensile tests. Based on current research on deformation mechanisms in UFG and nc materials, we will review some of the following aspects.

### 2.3.1. Size effect on plasticity

In single-phase bulk nc materials, it is likely that for the larger end of the nanoscale grain sizes, about 50 to 100 nm, dislocation activity dominates for test temperatures  $< 0.5 T_m$ , where  $T_m$  stands for melting temperature of the material. As grain size decreases (still larger than 10 nm), dislocation activity decreases due to the reduction of dislocation density in small nc grains. In other word, intragrain deformation, evidenced mainly by dislocation activity, dominates at these stages (10-100 nm). At the smallest grain sizes regimes, 10 nm or less, a new deformation mechanism might dominate, intergrain deformation, which may involve grain boundary sliding or grain rotation accompanied by short-range diffusion assisted healing events. Grain boundary sliding was predicted by molecular dynamics (MD) simulations [66-68] and observed experimentally [69,70]. Moreover, MD simulations have shown that grain boundary sliding might be triggered by atomic shuffling and to a minor extent, stress assisted free volume migration [68]. Atomic shuffling involves short range atomic motion in which an atom shifts from a position associated with one grain orientation to a position associated with another neighboring grain orientation or an intermediate one [68]. This is a non-diffusional process, as it does not involve long-range mass transport. Chen *et al.* [71] determined the critical shear stress to initiate plasticity in nc Cu (average grain size is around 14 nm) with nanoindentation technique. The measured critical shear stress, around 8 GPa, is identical to that required for the nucleation of lattice dislocations in cg Cu, close to the theoretical strength in dislocation free single crystal Cu. Their studies, consistent with MD simulations [72], indicate that the onset of plasticity of the nc Cu is associated with initiation of dislocation activities at grain boundaries.

The grain size effect on plasticity is also reflected from the strength of these materials. In the typical Hall-Petch plot, hardness vs.  $1/d^{-1/2}$  ( $d$  is the average grain size), the hardness usually increases linearly with  $1/d^{-1/2}$  for grain size larger than 100 nm. Dislocation pile-up model can explain the strength-

ening behavior in this regime. This linear strengthening relation is deviated, with hardness falling below the value predicted by the extension of linear relation, at smaller grain sizes, 10 ~ 100 nm. Dislocation pile-ups become less likely in this range. Instead, dislocation bowing mechanism, Orowan model, may start to operate [73,74]. The hardness typically reaches its maximum at around 10 nm, where dislocation activities mainly originate from grain boundaries. Misra *et al.* [75,76] propose a single dislocation model to explain the strengthening in multilayer composites when the layer thickness is in the nanoscale, 100 nm or less. The model predicts an increase in strength of the multilayer with decreasing layer thickness of each individual layer, consistent with experimental observations.

### 2.3.2. Ductility

Although nc metals have significantly higher strength than cg materials, their ductility is often limited. Ductility can be measured via many techniques. Uniaxial tensile tests are most frequently used for measuring ductility in conventional materials as they provide rich information about deformation mechanisms of the materials, such as strain hardening and strain rate sensitivity.

**Strain hardening.** During plastic deformation of conventional metals and alloys, the flow stress required to produce slip continuously increases with increasing strain. This effect, known as strain hardening or work hardening, is usually caused by dislocations interacting with each other or with barriers which impede their motion through the crystal lattice. Strain hardening is an important behavior often observed in ductile deformation. An ideal plastic material, where there is no strain hardening, would become unstable and start necking as soon as yielding occurs. The condition of tensile instability is described as:  $(d\sigma/d\varepsilon) < \sigma$ , where  $\sigma$  and  $\varepsilon$  stands for flow stress and strain during deformation.

Research on strain hardening behavior in ufg and nc materials is somewhat controversial. In some cases, ufg and nc materials are found to show strong strain hardening behaviors [11,14,78,79], whereas in other cases, they show little strain hardening [80-83]. Careful examinations of these studies are necessary as the difference in these studies lie in many factors such as processing techniques, microstructure, density and testing techniques.

**Strain rate sensitivity.** Strain rate,  $\dot{\varepsilon}$  is defined as  $d\varepsilon/dt$  and is expressed in units of  $s^{-1}$ . Strain rate has an important effect on the flow stress. At constant strain and temperature, a general relationship between flow stress and strain rate is:

$$\sigma = C(\dot{\varepsilon})^m, \quad (5)$$

where  $C$  is a constant and  $m$  is known as the strain rate sensitivity.  $m$  can be calculated by:

$$m = \left( \frac{\partial \ln \sigma}{\partial \ln \dot{\varepsilon}} \right) = \frac{\log(\sigma_2/\sigma_1)}{\log(\dot{\varepsilon}_1/\dot{\varepsilon}_2)}. \quad (6)$$

Therefore, the exponent  $m$  can be obtained from a plot of  $\log \sigma$  vs.  $\log \dot{\varepsilon}$ . The value of  $m$  conveys information of deformation mechanisms related to dislocation activity and/or grain boundary sliding [84]. Strain rate sensitivity of metals is usually low ( $m < 0.2$ ) at room temperature but  $m$  increases with testing temperature. A more sensitive way to obtain  $m$ , is a rate change test or jump test, in which  $m$  is determined by measuring the change in flow stress brought about by a change in  $\dot{\varepsilon}$  at a constant strain and temperature.

Mechanical properties of certain ufg and nc materials are found to be more sensitive to strain rate than their cg counterparts [57,81,85]. High strain rate sensitivity, typically  $> 0.33$ , is a characteristic of superplastic metals and alloys. Superplasticity refers to extreme extensibility with elongations usually between 100 and 1000 percent [84]. There are some examples where ufg or nc elemental metals possess superplastic behavior [86], but it has characteristics different from those of micron grain size materials.

By systematic studies of plastic deformation of ufg and nc materials as a function of testing temperature, strain rate, and grain size in artifact free samples, it is possible to obtain an improved understanding of the deformation and fracture mechanisms in these materials. This understanding can

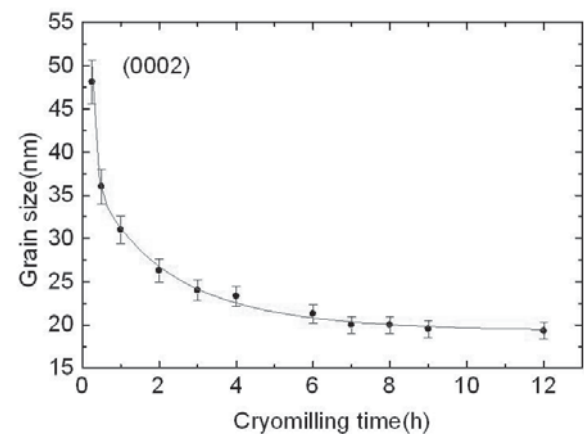


**Fig. 3.** X-ray result of grain size vs. cryomilling time for CM Zn.

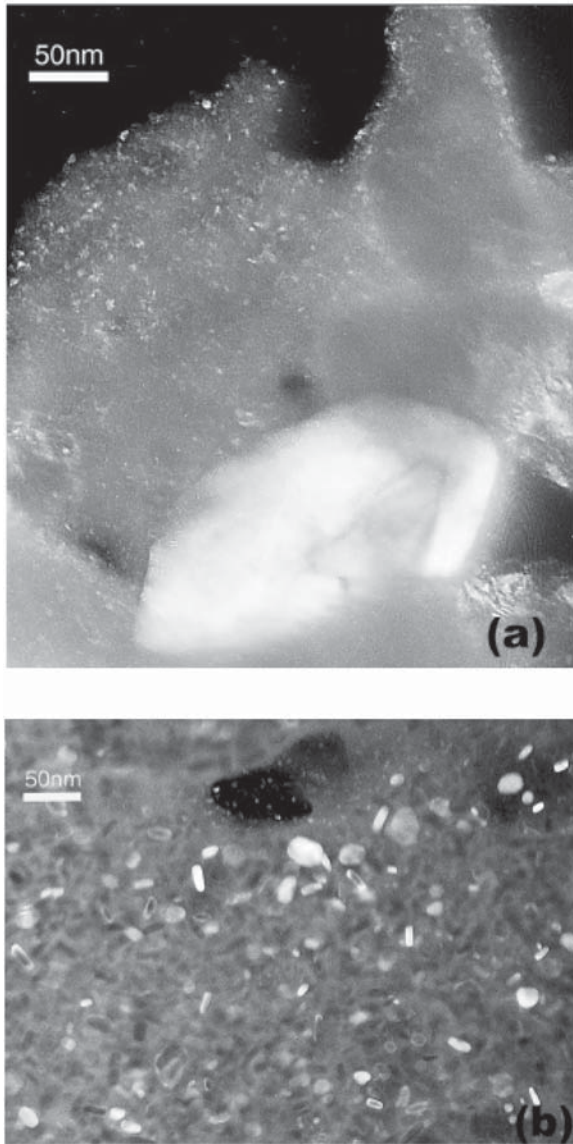


**Fig. 4.** (a) TEM dark field image for CM0.5h Zn. (b) TEM dark field image for CM12h Zn.

be greatly assisted by careful examination of microstructures before and after tests such as grain boundary structure, dislocation density, grain size and its distributions.

### 3. MICROSTRUCTURE EVOLUTION IN CRYOMILLED Zn

#### 3.1. Nanocrystallite formation by dynamic recrystallization

**Evolution of average grain size and grain size distributions.** The average grain size of CM Zn estimated by using (0002) type X-ray diffraction line

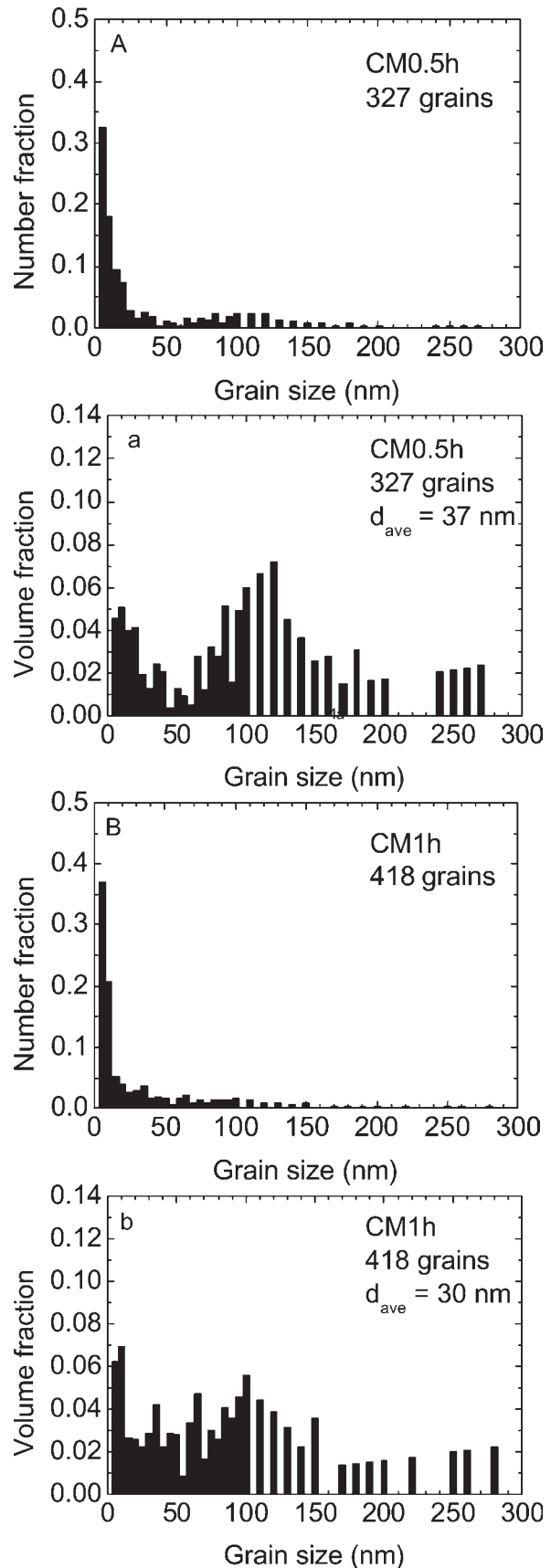


**Fig. 5.** The number fraction and volume fraction of grains vs. grain sizes at different cryomilling time. 5A-5E stands for number fraction and 5a-5e stands for volume fraction for CM0.5h, CM1h, CM3h, CM6h, and CM12h.

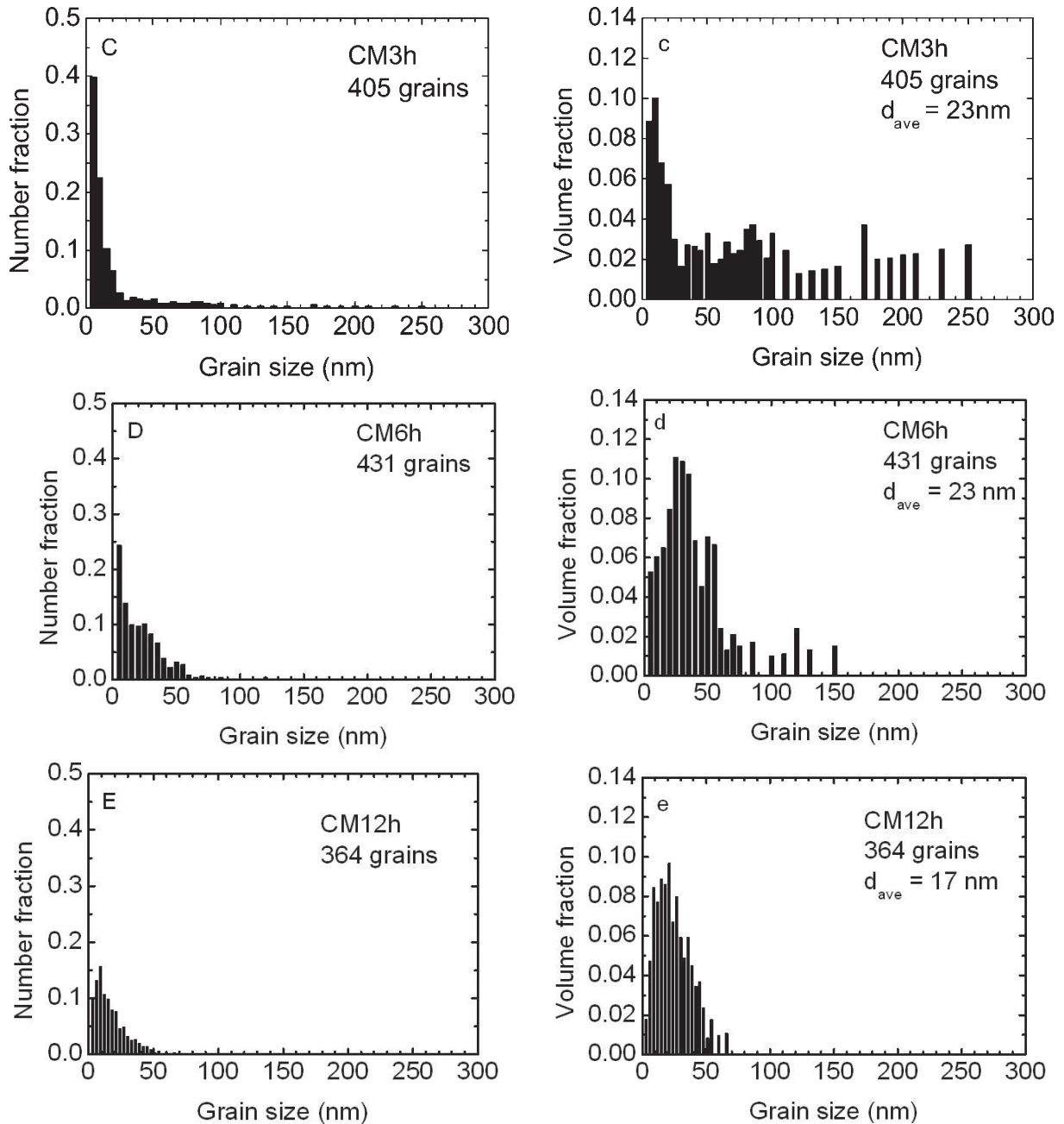


Fig. 5. Continued.

broadening [35,36], gave values which decreased rapidly during the first hours of milling and then slowly decreased to a nearly constant value for longer milling times as shown in Fig. 3. The grain size clearly saturates to the minimum value of about 20nm after about 12 h of milling. All the Zn samples after cryomilling were still in the powder form. The evolution of average grain size with milling time is somewhat typical for many other ball milled metals.

Transmission electron microscopy (TEM) studies of CM Zn provide more insight into the evolution

of grain size distribution during milling. Fig. 4a shows the TEM dark field images of the CM0.5h Zn. Large grains of about 250 nm exist together with small grains of less than 10 nm. Fig. 4b shows the TEM dark field images of the CM12h Zn specimen. It is clear that the grain size is much more uniformly distributed. Fig. 5 shows the results of number fraction (5A-5E) and volume fraction (5a-5e) of grain sizes of the CM Zn calculated from TEM studies. It is surprising to see a large fraction of nc grains, less than 5 nm with a number fraction of about 30%,

**Table 1.** A comparison of grain sizes calculated from TEM and X-ray studies.

	Grain size (nm)	
	TEM result	X-ray result
CM 0.5 h	37±1	36±2
CM 1h	30±1	31±2
CM 3h	23±1	24±2
CM 6h	23±1	21±1
CM 12h	17±1	19±1

even in an early stage (0.5h) of cryomilling as shown in Fig. 5a. The corresponding volume distribution of the grain size shows that these small grains do not contribute to the total volume as much as they do to the number fraction distribution. Large grains (>50 nm) comprised more than 75% of the total volume of the grains. The grain size distribution (volume fraction) tends to be bimodal in Figs. 5a – 5c, where one peak exists in the small grain size regime and the other broad and higher peak lies in in the large grain size regime. This tendency is reduced after 6 h milling, i.e., after 6 h cryomilling, there is only one peak, though still broad, in the volume fraction grain size distribution as presented in Fig. 5d. After 12 h cryomilling, only one narrower peak exists in both the number fraction and volume fraction curves as seen in Fig. 5e. This shows that the grain size has been reduced to a uniformly small and saturation value, i.e. the average minimum grain size has been reached after 12 h cryomilling. At this stage, about 98% of the grains were less than 60 nm in diameter.

Table 1 gives the values of average grain size calculated from X-ray and TEM (from the volume fraction result). It shows that the average grain sizes calculated from these two methods are consistent with each other, even if the close agreement may be fortuitous given the approximate nature of the XRD line broadening method. The  $d_{min}$  of Zn induced by cryomilling was about 17 nm (according to the TEM results for CM12h Zn). It is in a similar range, although slightly larger, compared to other hcp metals (about 14 nm for Co, Hf and Ru) [21]. This may be understood since Zn has a fairly low melting point ( $T_m = 692.6\text{K}$ ), which might lead to relatively higher  $d_{min}$  than other hcp metals that have been studied with much higher  $T_m$ . According to Eq. (1), the critical equilibrium distance ( $L_c$ ) between two edge dislocations in a pile-up was calculated to be about 15 nm for Zn. This is consistent with the minimum average grain size of Zn.

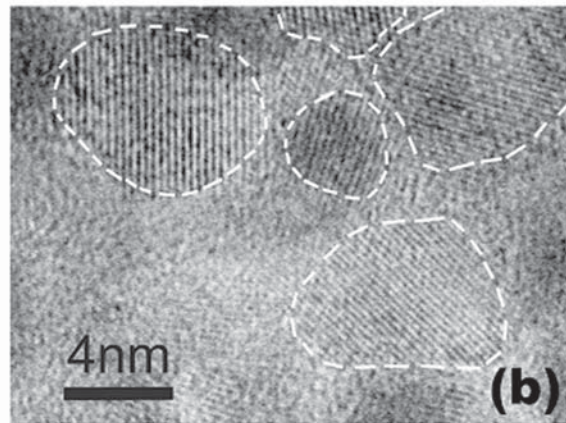
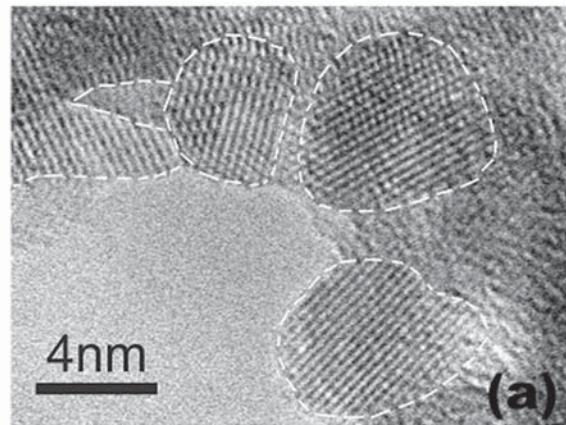


**Fig. 6.** (a) High resolution transmission electron microscopy (HRTEM) image of CM0.5h Zn. (b) HRTEM image of CM12h Zn.

The microscopic characteristics of small nc grains obtained during the early cryomilling stage, CM0.5h, are quite similar to those of nc grains obtained after a much longer milling time, CM12h. As shown in Fig. 6a studied by high resolution transmission electron microscopy (HRTEM), small grains, about 4 nm in diameter, induced by 0.5 h of cryomilling also possess high angle grain boundaries, which is the typical characteristic of nc grains in CM 12h Zn.

The mechanism proposed by Fecht [16] may explain the gradual decrease of the volume fraction of the large grains (~ 100 nm). This mechanism, however, has some difficulties in explaining the generation of a large number of small grains (around 5 nm) in the early cryomilling stages. At this milling stage, according to the Fecht mechanism, subgrains around 20 nm with low angle grain boundaries could be formed [16].

**The formation of small nc grains in CM Zn by dynamic recrystallization.** Mechanical milling will usually create a high strain and high dislocation density similar to some traditional cold working techniques. The energy induced by cold working is usually stored in the high dislocation density regions or regions with high strain levels. The stored energy will be greater for large strains. At low to medium strain levels (generally  $< 1.0$ ), and at normal strain rates, metals deform by slip or twinning and at somewhat higher strain levels instabilities develop and shear bands form [87]. Shear bands of all types provide favored sites for the nucleation of recrystallized grains. Ridha and Hutchinson [88] have shown that after annealing, nuclei having a wide range of orientations develop in the shear bands. Shear bands have been found in Zn which was induced by severe cold rolling [89]. DRX happened within the shear bands at room temperature. Compared to cold rolling, cryomilling may induce much higher strain into the deformed metals, thus creating some highly strained regions. These highly strained areas may have stored enough energy to promote the nucleation of nc Zn grains during the cryomilling process.

A critical requirement for nucleation is that the surface of the recrystallized grain nucleus must be a mobile grain boundary, i.e. high angle grain boundary [90]. Several possible nucleation mechanisms have been proposed [38,45]. Though different from each other, they all suggest that the nucleation happens in certain locations of the deformed microstructure, in particular in deformation inhomogeneities like shear bands or microbands, where there is a high dislocation density. The critical nucleation diameter for DRX has also been closely related to the dislocation density and strain rate as shown in Eq. (2) in Sec. 2.1.4. It follows that the ratio of dislocation density (power 3) over strain rate has to achieve a certain value in order to form the critical nucleus diameter, see Eq. (4) in Sec. 2.1.4. However, in some materials deformed at room temperature, dynamic recovery usually happens simultaneously with defect creation so the dislocation density cannot reach this value. But in the current case, the dynamic recovery rate may be well depressed by the low milling temperature, thus decreasing the dislocation recombination rate allowing the achievement of the critical nucleus radius. However, the critical nucleus radius may be only a few nm for the formation of nc grains, which therefore may not need as high a dislocation density to promote nucleation as traditional materials do.

The DRX mechanism can also be understood from the thermodynamic point of view. During the

ball milling process, the plastic damage in the form of dislocations is generated via high strain rate impacts from the balls. As the milling time increases, the dislocation density continues to increase. This critical value of dislocation density  $\rho_c$  is given by  $NE_d/E_d$ , where  $N$  is the atomic density,  $E_c$  is the recrystallization energy and  $E_d$  is the total dislocation energy per unit length including the core energy of the dislocation. For micro-erosion, a rough estimate in silicon, shows that for around  $6 \cdot 10^{11}$   $\text{cm}^{-2}$  dislocation density, the average energy stored in dislocations reaches about 0.1 eV/atom, which is close to the amorphous-to-crystalline crystallization energy [91]. It is envisaged that at these levels of dislocation density, small energy fluctuations resulting from impacts during the milling process can trigger a DRX event. This DRX event leads to formation of nc grains with orientations different from the original grain orientation.

Based on the DRX mechanism, the bimodal grain size distribution in the early stage of milling may be understood. We assume that the peak in the small grain size distribution in Figs. 5a – 5c has been induced by DRX. That is, the small grains around 5 nm as shown in the Fig. 6a and Fig. 6b are grains created by DRX. Such small grains will not grow significantly (usually to less than 20 nm) because of nucleation of additional grains at the migrating boundaries [38]. On the other hand, the decomposition of the very large grains may follow a mechanism similar to that described by Fecht [16]. Within the large grains the subgrains are usually on the scale of 20 nm. The broad grain size distribution at early cryomilling stages ( $< 6$  h) suggests that these two mechanisms may operate simultaneously. After certain cryomilling times [20] the broad grain size distribution becomes a single narrow peak, which implies a dynamic equilibrium has been reached.

### 3. 2. Lattice strain and stored enthalpy

The lattice strains of three different types of planes, (0002)  $(10\bar{1}0)$   $(10\bar{1}1)$ , calculated by the approach of Williamson and Hall [35], are plotted vs. milling time in Fig. 7. It is seen that the lattice strains rise rapidly to about 0.15% for  $(10\bar{1}0)$  and  $(10\bar{1}1)$  type planes after 1 h of milling. Thereafter, they drop rapidly and approach zero for longer milling time. The lattice strain for (0002) type planes continues to increase with milling time, reaches a maximum value of 0.48% after 6 h of milling and then decreases, almost linearly, with milling time to a small value of about 0.05% at 12 h. The fact that the larger values

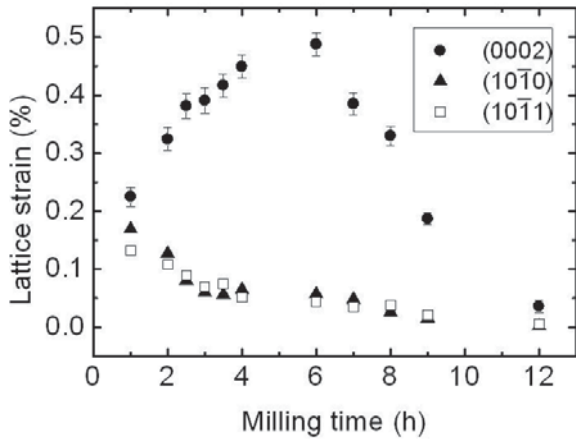


**Fig. 7.** Lattice strain vs. cryomilling time for three types of lattice planes, (0002) (10 $\bar{1}0$ ) (10 $\bar{1}1$ ).

of lattice strain are observed for the (0002) type reflections suggests that the lattice strain comes mainly from the basal plane. This is reasonable, since the predominant slip system for Zn is  $\{0001\} \langle 11\bar{2}0 \rangle$  [92]. For Zn, the  $c/a$  ratio is 1.856, which is much larger than the ideal value of 1.633 for the hcp structure. Thus basal plane slip is favored. Dislocations are confined to the closely packed basal plane and do not move freely from it [38]. The magnitude of lattice strain is a good indication of dislocation density within the materials. Thus the variation of lattice strain with cryomilling time indicates the change of dislocation density in the system.

Thermal stability of the CM Zn was studied by differential scanning calorimeter (DSC). Figs. 8a-8d show the DSC heat flow vs. temperature plots (at a constant heating rate of 40 °C/min) for Zn cryomilled for 1, 3, 6, and 9 h respectively. For 1 h milling time (Fig. 8a), two broad exothermic peaks (a low temperature peak and a high temperature peak) are evident at about 195 °C and 295 °C with another peak (middle peak) following the low temperature peak closely at 245 °C. After 3h of milling (Fig. 8b) the peaks at 195 °C and 245 °C appear to merge into a single broad peak at about 210 °C. The second DSC peak drops in temperature somewhat to about 285 °C. Continued milling to 6 h gives what appears to be a single broad peak at about 200 °C (Fig. 8c) and little evidence for the second peak, which can be revealed only at higher DSC heating rates ( $\geq 60$  °C/min). No obvious peaks are evident over the temperature range up to 350 °C after 9 h of milling (Fig. 8d). The thermal stability studies of CM Zn will focus on the low temperature peak, referred to as the LT peak. Details on high temperature peak can be found in ref. [93].

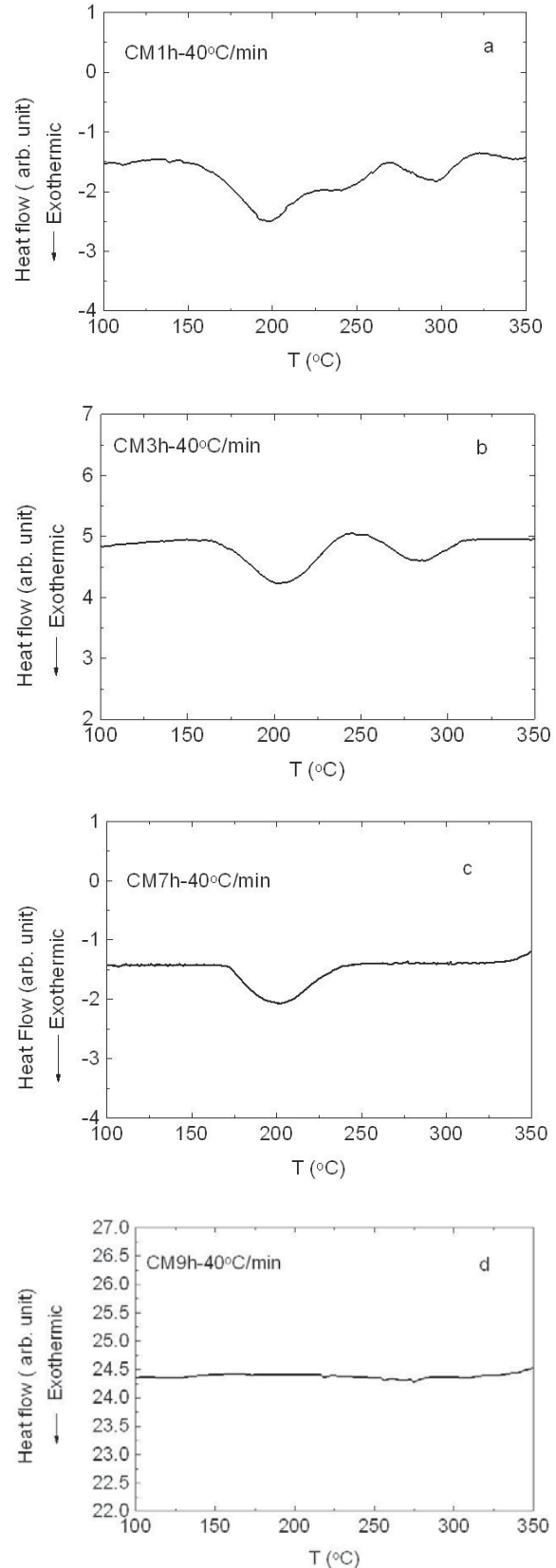


**Fig. 8.** DSC thermograms for Zn cryomilled at 77K for (a)1 h, (b) 3 h, (c) 7 h, and (d) 9h.

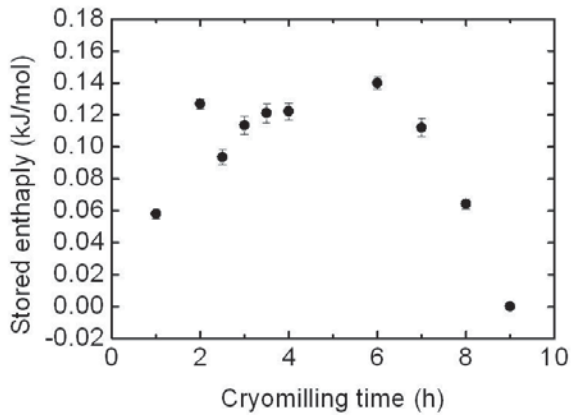


**Fig. 9.** Stored enthalpy of LT DSC exothermic peak vs. cryomilling time.

The exothermic heat associated with the LT peak (around 200 °C) was calculated from the area under the peak. This stored enthalpy so released (measured at a constant heating rate of 40 °C/min) is plotted vs. milling time in Fig. 9. The stored enthalpy increases to a maximum of 0.14 kJ/mol after 6 h of milling and then decreases rapidly to zero at 9 h of milling. The relatively high stored enthalpy after cryomilling for 2 h may be due to the overlapping of the LT peak and the middle peak.

In order to assess the source of the exothermic peaks observed in the DSC scans, annealing was carried out in the DSC by heating the selected samples to the certain temperatures with the same heating rate of 40 °C/min and then cooling down immediately. The evolution of lattice strain and average grain size was studied by XRD for three sets of planes. As shown in Fig. 10, in all cases, there is hardly detectable grain growth from below 245 °C, which is the finishing temperature for the LT DSC peak. The lattice strain in the (0002) type planes, however, dropped by about a factor of two after the

**Table 2.** A comparison of grain size calculated from TEM (average grain size estimated from the volume fraction distribution) and X-ray (0002) type planes for CM3h sample annealed at different temperatures.

Annealing temperature (°C)	Grain size (nm)	
	TEM result	X-ray result
as milled (23)	23±2	24±2
142	24±3	24±2
245	27±2	26±2

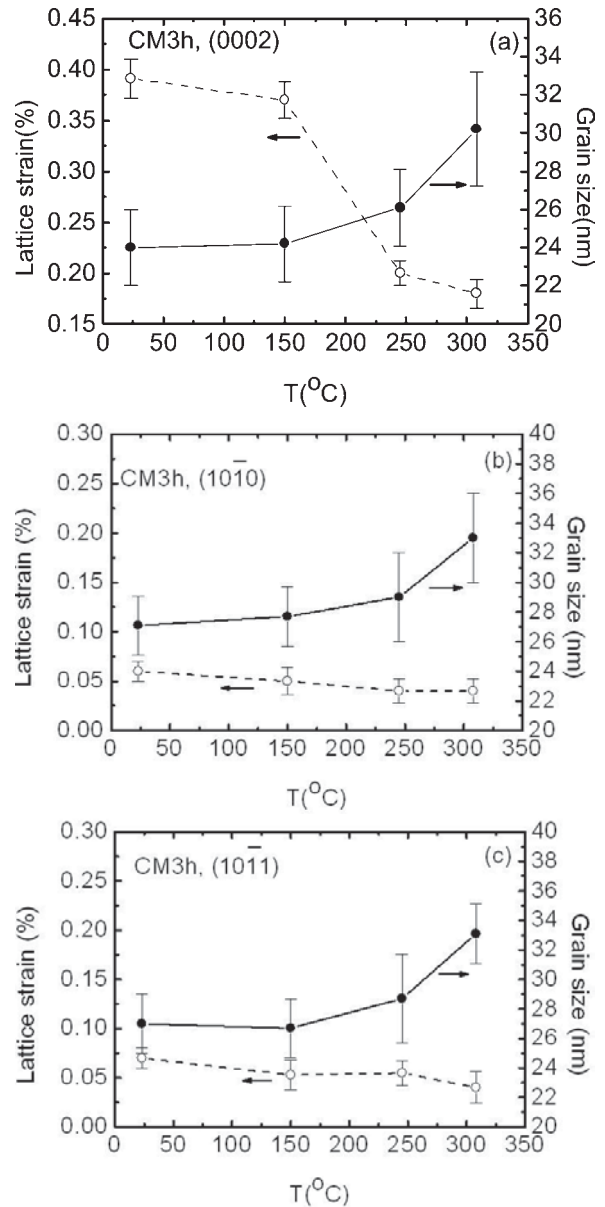


**Fig. 10.** Lattice strain and grain size vs. annealing temperature for (a) (0002) type planes, (b) (10 $\bar{1}$ 0) type planes, (c) (10 $\bar{1}$ 1) type planes for CM3h sample.

annealing period of LT DSC peak. Whereas the reduction of lattice strain on the (10 $\bar{1}$ 0) and (10 $\bar{1}$ 1) planes during the same annealing period is not as significant as that in the (0002) plane. TEM studies of the annealed CM3h Zn specimens, as shown in Fig. 11, confirmed that there is very little variation of the average grain size, (the average grain size data are compared with that calculated from XRD in Table 2) for annealing below 245 °C.

The above studies indicate that the contribution of grain growth to stored enthalpy measured in LT DSC peak is negligible. The reduction of lattice strain

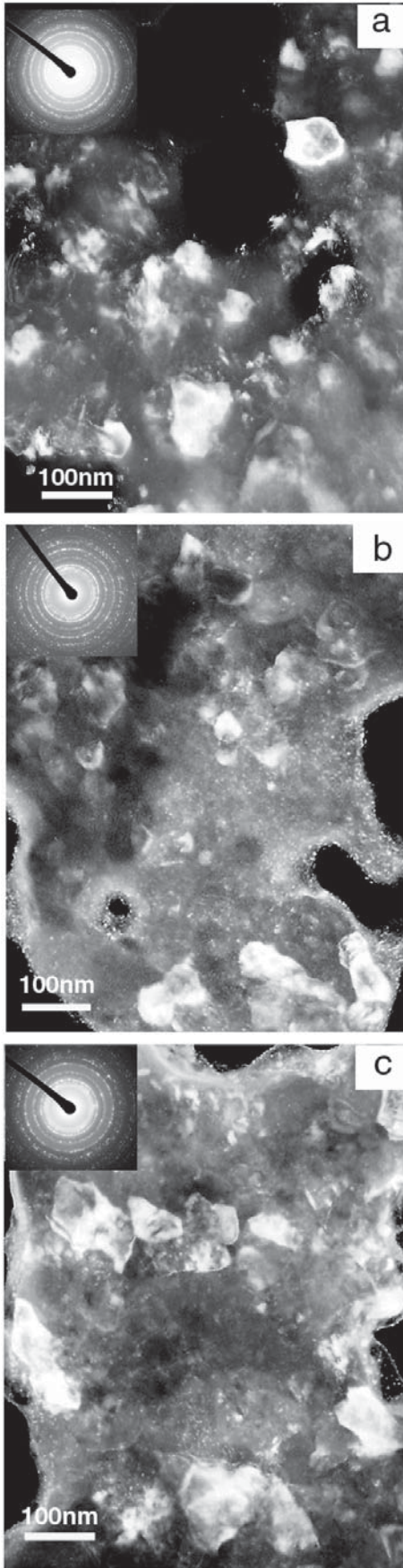


**Fig. 11.** TEM dark field images of grain size after annealing at different temperatures for CM3h Zn. (a) 23 °C, (b) 142 °C, (c) 245 °C.

on (0002) type planes during annealing indicates the decrease of dislocation density. Plastic deformation induced by the cryomilling process can create a very high dislocation density. The stored energy due to dislocations is proportional to the dislocation density ( $\rho$ ) as shown in the following equations [94]:

$$E_D = \rho E_{dis}, \quad (7)$$

$$E_{dis} = \frac{Gb^2 f(\nu)}{4\pi} \ln\left(\frac{\alpha R}{2b}\right), \quad (8)$$

where  $E_D$  is the total strain energy of the dislocation,  $E_{dis}$  is the strain energy of the dislocation per unit length,  $G$  is the shear modulus,  $b$  is the magnitude of the Burgers vector,  $f(\nu)$  is a function of Poisson's ratio,  $f(\nu) = (1-\nu/2)/(1-\nu)$  with considerations of both screw dislocations and edge dislocations,  $R$  is the separation between the dislocations,  $a$  is the core energy factor close to unity [95].

For nc Zn, assume that the maximum dislocation density ( $\rho$ ) reachable is of the order of  $10^{15}/\text{m}^2$ , which is a reasonable assumption compared with dislocation densities reached in other pure metals deformed at 77K [96]. Taking  $G = 49.3$  GPa,  $b = 0.267$  nm,  $\nu = 0.3$ ,  $\rho = 10^{15}/\text{m}^2$ ,  $R = \rho^{-1/2}$ ,  $\alpha = 1$ ,  $E_D$  is calculated to be about 120 J/mol, which is very close to the measured maximum stored enthalpy of 110 J/mol for the CM3h Zn. This suggests that the majority of the stored enthalpy may originate from the high density of dislocations induced by high-energy cryomilling.

Variation of the stored enthalpy (for the first peak) and lattice strain on the basal plane were plotted

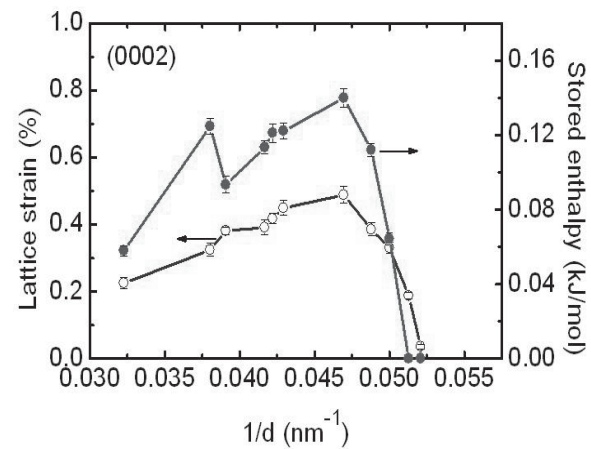


**Fig. 12.** Stored enthalpy (lower temperature peak) and lattice strain on the basal plane vs.  $1/d$ , where  $d$  is the grain size.

together vs. the reciprocal of the average grain size ( $1/d$ ) in Fig. 12. In contrast to some other observations on other elements [26], Fig. 12 clearly shows that maxima in both stored enthalpy and lattice strain occur at the same grain size. The consistency between the two maxima confirms that the change of stored enthalpy is dominated by variation of dislocation density during milling. Thus it suggests that the dislocation density increases during the initial cryomilling stage, reaches a maximum at around 6 h, and then decreases almost linearly with continuous cryomilling. It is generally believed that nc materials with grain sizes less than a certain value are dislocation free [69,70]. Therefore the reduction of dislocation density might be due to the increase of these dislocation-free nc grains.

The inconsistency between the maxima of stored enthalpy and lattice strain in certain systems [26] may be related to the cancellation of strains during milling. The strain field of dislocations could be cancelled out if dislocations with positive Burgers vector and others with negative Burgers vector are next to each other. The total lattice strains may be reduced due to this cancellation effect. But the dislocation energy is proportional to the square of the magnitude of Burgers vector according to Eq. (8). Thus the dislocations with either positive or negative Burgers vector will contribute to the stored enthalpy. For fcc and bcc metals, slip can occur on multiple (typically more than five) slip systems. The cancellation of strain field due to adjacent dislocations with positive and negative Burgers vector on multiple slip systems can be significant. This might explain the discrepancy of maximum of lattice strain and stored enthalpy occurring at different milling times observed in the bcc and fcc structured metals [19]. In the case of hcp metals, such as Zn, slip is mostly confined to the basal planes, the lattice strain may add up without a significant cancellation effect. Therefore, for Zn, the variation of lattice strain is consistent with the observed change of stored enthalpy, that is the lattice strain and stored enthalpy reach maxima at the same grain size.

Positions of the LT peak temperatures were seen to shift to higher temperatures with increased heating rates in the DSC. Heating rates were selected with a variation from 20 °C/min to 80 °C/min. This allowed for the Kissinger method [97] to be used to estimate activation energy values for the processes responsible for the exothermic peaks. The activation energy for samples cryomilled for different times is listed in Table 3. The activation energy for the LT peak is around 80 kJ/mol. This is in between the activation energy for grain boundary self diffusion in

Zn of 59 kJ/mol [98], and lattice self diffusion in Zn of 96 kJ/mol [99]. The dislocations are distributed both within the larger nc grains and at the grain boundaries. During the annealing process, the annihilation and movement of these dislocations may have different activation energies. Dislocations located at the grain boundaries need less activation energy to annihilate with each other, while those located within grains may need higher activation energy to move. Therefore the annealing processes in this temperature range might be correlated with both grain boundary diffusion and lattice diffusion processes.

## 4. MECHANICAL BEHAVIOR OF CRYOMILLED BULK NC Zn

### 4.1. Effect of dynamic recrystallization on the mechanical behavior of compacted bulk CM Zn

#### *Evolution of hardness with milling time.*

Cryomilled nc Zn powders were compacted at room temperature in an attempt to test their mechanical properties, such as strength and ductility. The measured density and hardness values for CMZn are plotted in Fig. 13 as a function of milling time. A relative density greater than 98% (0.98) of theoretical density was obtained for all of the CMZn samples. Fig. 13 shows that the CMZn hardness undergoes marked oscillations as a function of milling time. The magnitude of the hardness peaks decreases with milling time, thus exhibiting a modulated cyclic hardening manifest as damped oscillations of the hardness. At longer milling times the hardness reaches a steady-state value about twice that of unmilled Zn. Impurity concentration as a function of milling time, given in Table 4, did not exhibit cyclic behavior. The oxygen concentration was found to increase steadily from about 0.11 at.% for as-received Zn to 0.956 at.% after 12 h. The (negligible)

**Table 3.** Activation energy calculated from the peak temperature by Kissinger plot for the LT peak,  $E_{LT}$ .

Milling time (h)	$E_{LT}$ (KJ/mol)
1	84
2	75
3	81
4	79
6	72
7	82
8	85

**Table 4.** Quantitative chemical analysis of oxygen and iron impurities in the as-received and some cryomilled Zn samples.

Sample	Oxygen (at.%)	Iron (at.%)
as-received Zn	0.115	N/A
CM 2h	0.238	0.012
CM 6h	0.614	0.015
CM12h	0.956	0.028

Fe impurity concentration likewise increased monotonically from 0.012 at.% at 2 h milling to 0.028 at.% at 12 h. Therefore it is unlikely that the hardness oscillation is related with the impurities picked up during milling.

**Evolution of microstructure (dislocation density, grain size and its distribution) with milling time.** TEM bright field micrographs are shown in Fig. 14 for samples milled between 0.25 and 3 hours. A high dislocation density was observed in larger size grains (Figs. 14a and 14d), typically with grain sizes > 50 nm. In contrast, few dislocations could be observed for grain sizes < 50 nm (Fig. 14b), and dislocations were clearly absent in the smallest grains. These observations indicate that a grain size of 50 nm is a reasonable demarcation value above which strain hardening can produce high dislocation densities during milling and below which dislocation generation and strain hardening are not effective. Estimates made from HRTEM micrographs showed that the maximum dislocation density that could be achieved for grain sizes > 50 nm was on the order of  $10^{16} \text{ m}^{-2}$ . Fig. 14c shows a significant feature that was observed for those milling times where the hardness drops to its minimum values during the cyclic hardness variations. A profuse distribution of very small, dislocation-free grains has been formed within a single large grain after a milling time of 2 h. This corresponds to a hardness minimum for CMZn in Fig. 13, and the occurrence of a DRX effect is clearly suggested.

Detailed measurements of the grain-size distributions as a function of milling time can be found in Fig. 5. The volume fraction of grains with sizes larger than 50 nm is plotted against milling time in Fig. 15. It should be noted that intermittent drops were observed (arrows at open points) which coincide with the hardness oscillation minimum points for the first two peaks in Fig. 13. The volume fraction is temporarily reduced at these points because of the forma-

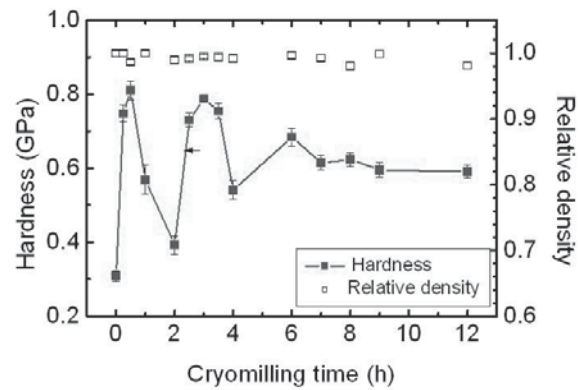


**Fig. 13.** Hardness vs. milling time for CM Zn (solid circles) The relative density for CMZn samples is shown by the open squares.

tion of a transient population of very small dislocation-free grains like those shown in Fig. 14c. These small grains subsequently grow and the overall decrease in the volume fraction of grains with a size > 50 nm is represented by the dashed trend line in Fig. 15.

**Theoretical simulation of hardness oscillation based on DRX model.** The DRX model follows the reaction-rate model proposed by Sluiter and Kawazoe [100]. The reaction-rate model was proposed to explain amorphous-to-crystalline phase transformations observed during ball milling [100]. In their model, it is assumed that ball milling increases the stored energy of the reactant phase due to defect accumulation. Once the activation energy for reaction (crystallization from amorphous phase) is surpassed, a reaction 'event' will occur with a sharply accelerating transformation rate. In the DRX model, we assume that dislocations produced by strain hardening in larger grains are the primary contribution to the stored energy in the DRX model. Based on the TEM observations, it is assumed that DRX occurs due to the accumulation of dislocations in grains with grain sizes larger than 50 nm (dislocations do not accumulate in smaller grains). Several important aspects have been captured by the DRX model:

- (i) the evolution of dislocation density. The stored dislocations will strengthen the materials by strain hardening.
- (ii) average grain size and grain size distributions. The gradual increase in hardening is related to average grain-size reduction during milling, i.e. Hall-Petch type hardening. Based on the assumption that dislocations will accumulate mainly in grains larger than 50 nm, the volume fraction

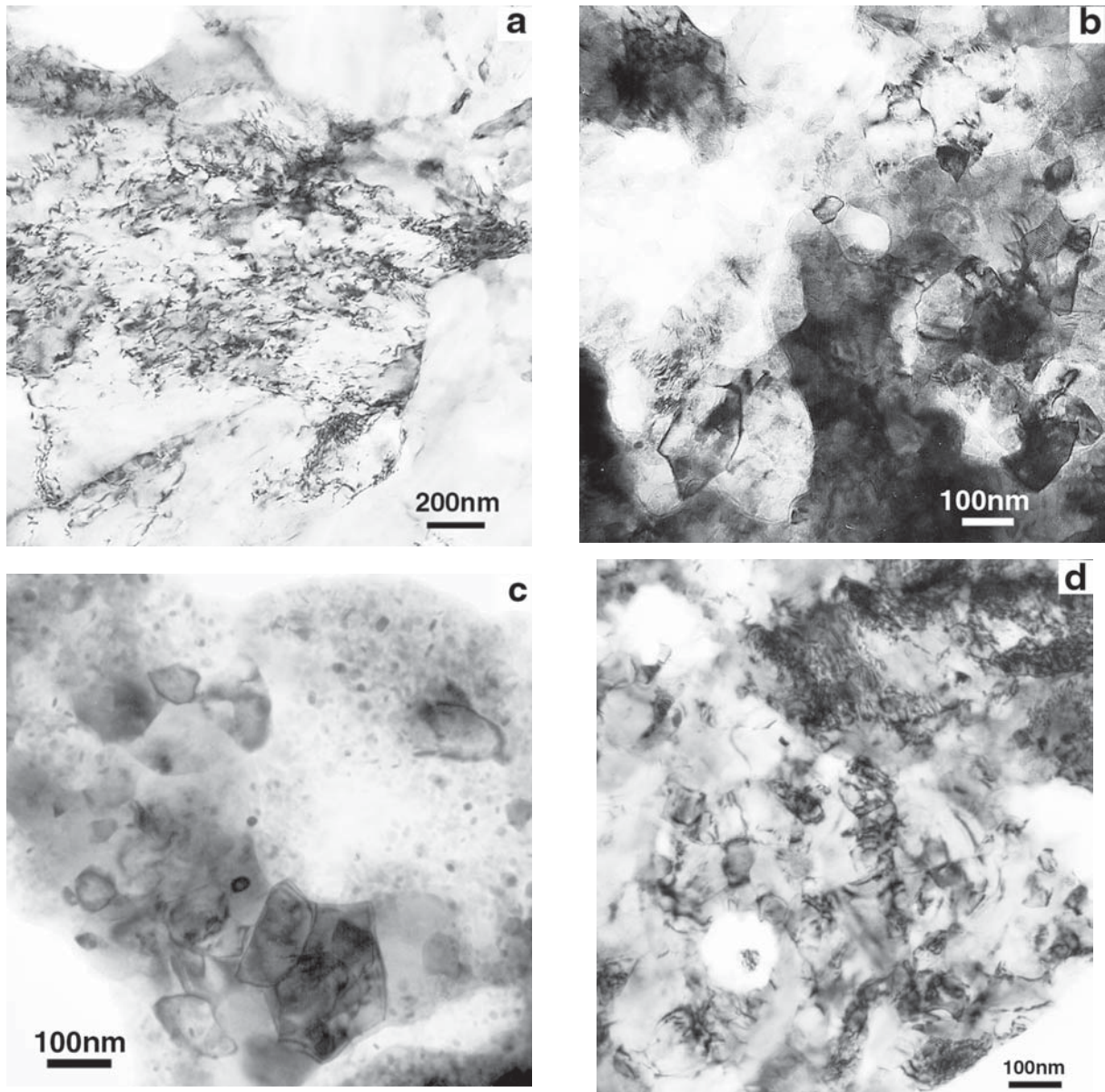


**Fig. 14.** TEM bright field images of CM Zn milled for different times: (a) 0.25 h, (b) 0.5 h (c) 2 h, (d) 3 h.

of grains larger than 50 nm will determine the extent of dislocation-induced strain hardening. (3) DRX events in the strain-hardened material produce modulated oscillations in hardness.

The strengthening in CM Zn eventually damp out as the volume fraction of grains with a size  $> 50$  nm is reduced at longer milling times. The details of DRX model can be found in ref. 101.

Fig. 16 shows the hardness data in Fig. 13 for CMZn plotted along with the results from the DRX model. The agreement is surprisingly good considering the simplifying assumptions needed to develop

the DRX model. The model overestimates somewhat the period (width) of the second peak and, especially, the third peak. This is due in large part to the lack of data points available to estimate the initial slopes and the hardening rate. Nonetheless, the fact that the hardness peak widths decrease as the initial slopes increase is clearly confirmed by the model. It is also noteworthy that the peak damping predicted by the model using as the scaling factor the volume fraction of grains with a size  $> 50$  nm is consistent with the CM Zn data.

The model presented here does not address the mechanisms that govern the actual DRX process in

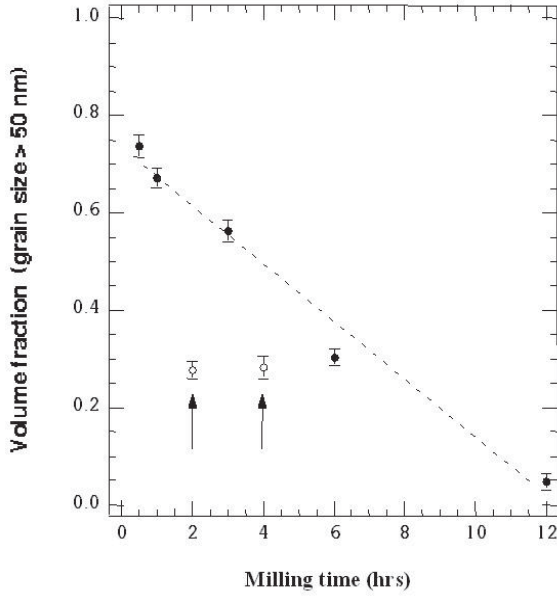


**Fig. 15.** Volume fraction of grain sizes > 50 nm vs. milling time for CMZn. Arrows (open points) indicate the positions of the hardness minimums for the first two peaks as shown in Fig. 13.

CMZn. However, the model does indicate that a critical strain-hardening dislocation density on the order of  $\rho_c \cong 10^{16} \text{ m}^{-2}$  (a critical parameter obtained by fitting experimental hardness data) will trigger DRX events in the larger grains. This upper limit for dislocation density is consistent with HRTEM estimates of the maximum dislocation density that could be observed in CM Zn samples [102].

Another important parameter that can be obtained from this model is the activation energy for kinetic reaction (or DRX). The best-fit value obtained for the reaction-rate parameter,  $K$ , was  $2 \cdot 10^{-4} \text{ s}^{-1}$ . A rough estimate of the activation energy (enthalpy)  $Q_0$  can be obtained from the value of  $K$  [101],

$$K = \nu e^{S_0/k} e^{Q_0/kT}, \quad (9)$$

where  $\nu$  is the attempt frequency,  $S_0$  is the activation entropy,  $k$  is the Boltzmann's constant. After rearranging this equation, one can derive that

$$Q_0 = -kT \ln \left( \frac{K}{\nu e^{S_0/k}} \right). \quad (10)$$

The attempt frequency for atom motion is on the order of the atomic jump frequency  $\nu \cong 10^{13} \text{ s}^{-1}$ . Assuming activation entropy to be on the order of  $S_0 =$

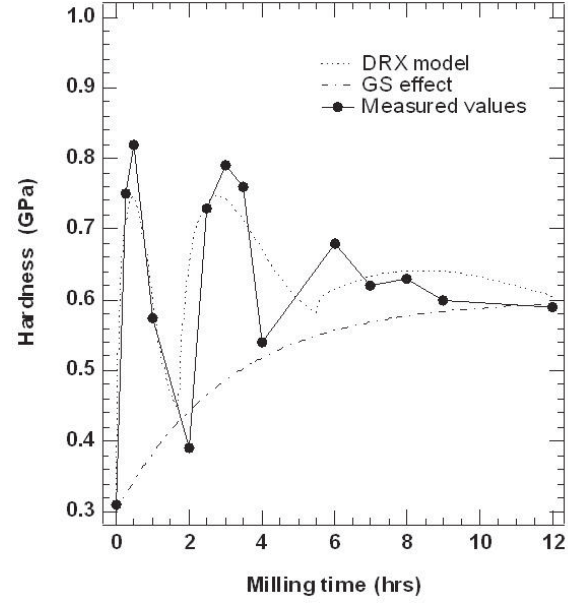


**Fig. 16.** Comparison of the DRX model results (dotted lines) with the experimental results of hardness vs. milling time for CM Zn (solid circles). The grain-boundary hardening (GS effect) is given by the dash-dot line.

$10 - 20k$ , and using  $K = 2 \cdot 10^{-4} \text{ s}^{-1}$  with  $T = 100 \text{ K}$  for cryomilling, Eq. (10) gives  $Q_0 = 40 - 50 \text{ kJ} \cdot \text{mol}^{-1}$ . The activation energy for grain-boundary diffusion in pure Zn is reported to be  $59 \text{ kJ} \cdot \text{mol}^{-1}$  [98]. The activation energy for the DRX process during cryomilling thus appears consistent with grain-boundary diffusion controlled atom mobility. This in turn would be consistent with grain-boundary migration processes, and these are expected to play an important role in DRX [45].

## 4. 2. Ductility of compacted bulk CM Zn

Strength and ductility of CM Zn were tested by miniaturized disk bend tests (MDBT). The details of this technique are given in the literature [103-106]. MDBT technique was originally developed to study the effects of fast neutron irradiation on the mechanical behavior of small specimens of reactor alloys [103-106]. Recently this technique has been improved and used for quantitative analysis of the mechanical behavior of nc materials [107, 108]. This technique has the advantage of testing in tension small samples produced by, for example, compaction of nc powders. Compared with conventional uniaxial tensile tests, MDBT is an equibiaxial tensile test technique. Therefore the strain measured from MDBT is equibiaxial tensile strain.

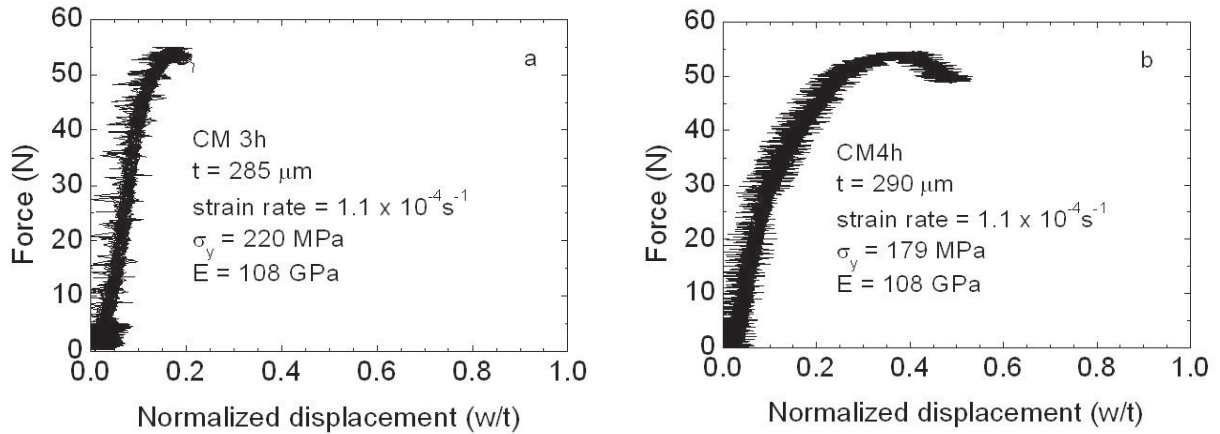


**Fig. 17.** Force vs. normalized displacement ( $w/t$ ) for selected samples tested by MDBT. (a) CM3h (b) CM4h. The symbol,  $\sigma_y$ , stands for yield stress, while  $E$  stands for Young's modulus.

Fig. 17 shows the force vs. normalized displacement curves for selected samples. Normalized displacement ( $\eta$ ) is expressed by  $w/t$ , where  $w$  is the displacement of specimen,  $t$  is the specimen thickness. Theoretical analysis shows that  $\eta$  is proportional to strain given all specimens have similar thicknesses [109]. Therefore the magnitude of  $\eta$  could provide an indication of the ductility of the specimen. As shown in Fig. 17a, CM 3h Zn has very limited  $\eta$  (about 18%) when the maximum force is reached. Whereas the CM4h Zn has a dramatic increase of  $\eta$  (about 40%) at the maximum of applied force, as presented in Fig. 17b. Both samples show plastic deformation. CM4h Zn has much more strain hardening than CM3h Zn specimen. The variations of yield stress,  $\sigma_y$ , and  $\varepsilon$  (calculated from force and displacement [109]) are plotted vs. cryomilling time in Fig. 18. It can be seen that both  $\varepsilon$  and  $\sigma_y$  show a modulated cyclic behavior with cryomilling time. Two maxima for  $\sigma_y$  are at CM0.5h and CM3h respectively, while two minima occur at CM2h and CM4h.  $\varepsilon$  varies in an opposite way with cryomilling time. That is, the peak of  $\varepsilon$  occurs where there is a minimum of  $\sigma_y$ . The low value of  $\varepsilon$  for all tested specimens may indicate the existence of two-dimensional flaws due to incomplete bonding between the powder particles. The fracture mechanism could be partly controlled by interparticle decohesion or powder-powder debonding. Given that all specimens have similar relative density, the number of two-dimensional flaws is, presumably, similar for all specimens. Therefore the variation of  $\varepsilon$  can still be used as a probe to compare the ductility of as-compacted Zn specimens. The results of microhardness,  $H_v$  and  $3\sigma_y$ , when plotted together vs. cryomilling time as

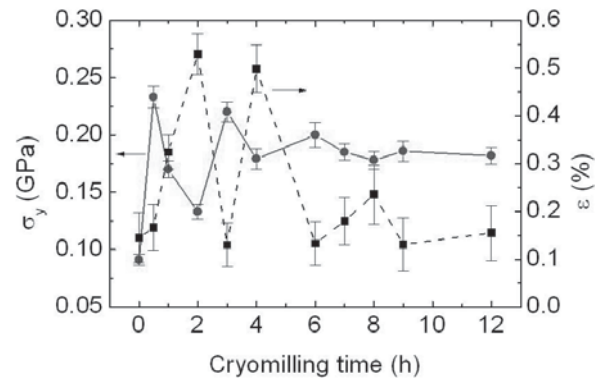


**Fig. 18.** Variations of yield stress ( $\sigma_y$ ) and strain ( $\varepsilon$ ) vs. cryomilling time for CM Zn.

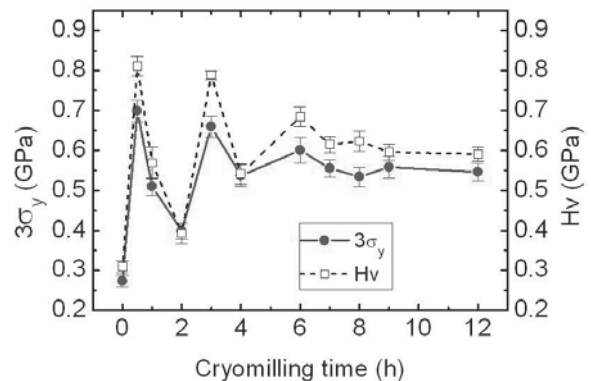


**Fig. 19.** Comparison of  $3\sigma_y$  and microhardness ( $H_v$ ) vs. cryomilling time for CM Zn.

given in Fig. 19, exhibit a coincident phenomenon both in the trend and magnitude of the variations. It is generally accepted that 3 times the yield strength is roughly the value of microhardness for the same materials. This empirical rule seems to work for Zn measured from MDBT.

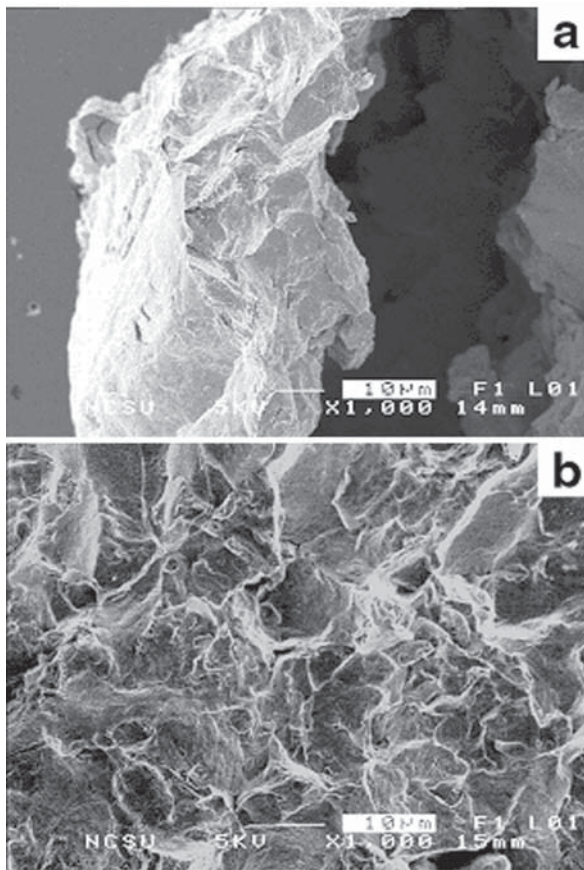


**Fig. 20.** FESEM observation of fracture surface of (a) CM0.5h Zn and (b) CM2h Zn after MDBT.

The morphology of the fracture surface of CM0.5h Zn and CM2h Zn samples after MDBT, studied by field emission scanning electron microscopy (FESEM), are shown in Fig. 20. The fracture surface of CM0.5h sample, as shown in Fig. 20a, shows certain brittle fracture features, with approximately a 10  $\mu\text{m}$  cleavage feature size. However, some ductile features, such as local tearing ridges, are also observed, indicating that these small regions may fracture by plastic flow. Tearing is frequently observed when small unbroken areas remain behind the main crack front. This suggests a mechanism of local fracture that is often found at a discontinuity in the crack advance by another fracture mechanism [110]. The fracture surface of CM2h Zn samples shows complex features on a rough surface as shown in Fig. 20b. Dimples, tearing ridges, as well as a number of quasicleavage features (shallow dimples) are observed on a macroscopic scale. These complex fracture features suggest that CM 2h Zn is much more ductile than CM0.5h Zn specimens. These

observations are consistent with the MDBT result, where the value of  $e$  of CM 2h Zn is about 3 times that of CM0.5h Zn.

It is observed from TEM that a broad bimodal grain size distribution exists for Zn cryomilled for less than 6h [17]. Grain size distribution, presumably, may also contribute to the deformation mechanisms and ductility of nc Zn. The phenomenological equation for grain boundary sliding controlled by grain boundary diffusion is given by [111, 112]

$$\dot{\epsilon} \approx 10^8 \left( \frac{\sigma}{E} \right) \frac{D_{gb} b}{d^3}, \quad (11)$$

where  $\sigma$  is the stress,  $D_{gb}$  is the grain boundary diffusion coefficient,  $b$  is the Burgers vector and  $d$  is the grain size. Eq. (11) suggests that for a very fine nanoscale grain size, grain boundary sliding may be a significant deformation mode even at relatively low temperatures. Therefore a broad grain size distribution indicates a complex mixture of deformation modes controlled by different grain sizes. This complexity will be reduced as the broad grain size distribution is replaced by a narrow single-peak grain size distribution for longer milling time.

## 5. THE SYNTHESIS OF BULK NC Zn BY *IN SITU* CONSOLIDATION OF POWDERS

Recently, bulk ufg and nc Zn were prepared by *in situ* consolidation of powders during milling at room temperature [113]. Pure Zn powders have been ball milled from 1 h up to 25 h at room temperature under ultra high purity argon. Only the original samples and the sample ball milled for 1 h (BM1h) are in the form of powders. All other samples ball milled for longer times are in form of  $\geq 1\text{mm}$  size spheres. Fig. 21 shows the Zn spheres induced by ball milling at different times. After 5 h of ball milling the sphere sizes varied from 2 mm to 5 mm. The sphere sizes increased to about 4 ~10 mm after 25 h of ball milling. The average size and the largest size of the spheres all increased with the increase of ball milling time. The appearance of these balls becomes more regular and uniform for longer milling times. It is well known that ball milling produces nanostructured materials by a severe plastic deformation process. During this process, the powder particles undergo a repetitive cold welding and fracture mechanism [8]. The fact that spherical balls are formed for Zn, Al and their alloys after ball milling at room temperature suggests that cold welding is predominant in these systems at room tempera-

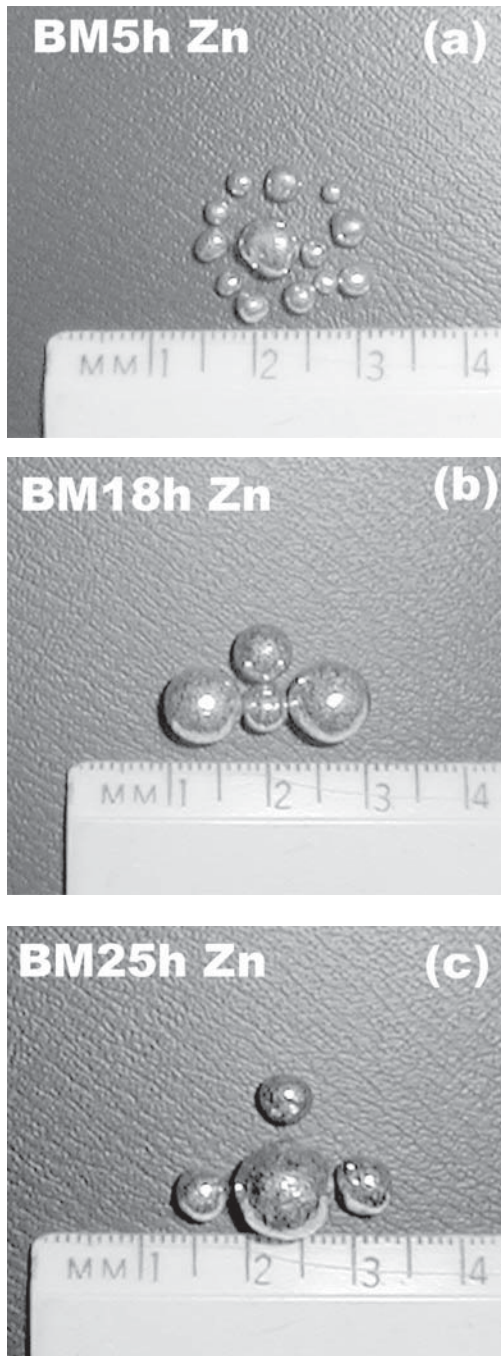


**Fig. 21.** Formation of spheres of pure Zn after milling for different times (a) 5 h, (b) 18 h, (c) 25 h.

ture. Spheres of nc copper have been synthesized by similar techniques and cold welding is believed to be predominant in this case as well [114,115].

The oxygen contamination of these Zn bulk samples is relatively small. As shown in Table 5, a maximum oxygen concentration of around 1 at.% was introduced after 25 h of ball milling. This is a modest amount of contamination compared with

other materials ball milled by high energy ball milling techniques [21]. The contamination from iron during the ball milling process is essentially negligible. Due to the ductile nature of these powders, a thin layer of powders formed on the surface of the stainless steel milling balls, thus reducing the possibility of further contamination from iron.

The evolution of grain size for BM Zn was studied with TEM. Some examples are given in Fig. 22 for Zn ball milled for 1h, 3h, 18h, and 25h. The evolution of volume fraction for these specimens, calculated from TEM micrographs, is presented in Fig. 23. A broad grain size distribution is observed in BM Zn in the early milling stages. The grain size of BM3h Zn varies from 5 to 500 nm. A bimodal grain size distribution is observed for BM1h Zn. Grain growth with continued milling is clearly seen from the comparison of the grain size distributions of BM1h and BM3h Zn. The grain size distribution becomes much narrower at longer milling time. After 25 h of ball milling, the grain size varies from 5 to 80 nm with an average value of 23 nm. The grain growth phenomenon in early milling stages has also been observed in several other materials [20,32]. In the case of BM Zn, it is possible that during the early milling stage, around 1 h, defect/dislocation generation dominates and therefore grain size is continuously refined. Between 1 and 3 h dynamic recovery dominates and grain growth is facilitated during this stage.

Zn spherical balls obtained by *in situ* consolidation can be compressed uniaxially at room temperature into a disk with a diameter of around 10 mm and thickness of about 1mm. The density of these disks was measured using the Archimedes principle method. In all cases, a relative density higher than 98% of theoretical density has been achieved. The bulk samples made from this technique are large enough (~ 10 mm in diameter) to perform many different kinds of mechanical tests, including the tensile test.

**Table 5.** Oxygen contamination in as-received and ball milled Zn samples.

Sample	Oxygen (at.%)
As-received (powder)	0.115
BM3h (sphere)	0.258
BM 5h (sphere)	0.296
BM 25h (sphere)	1.025

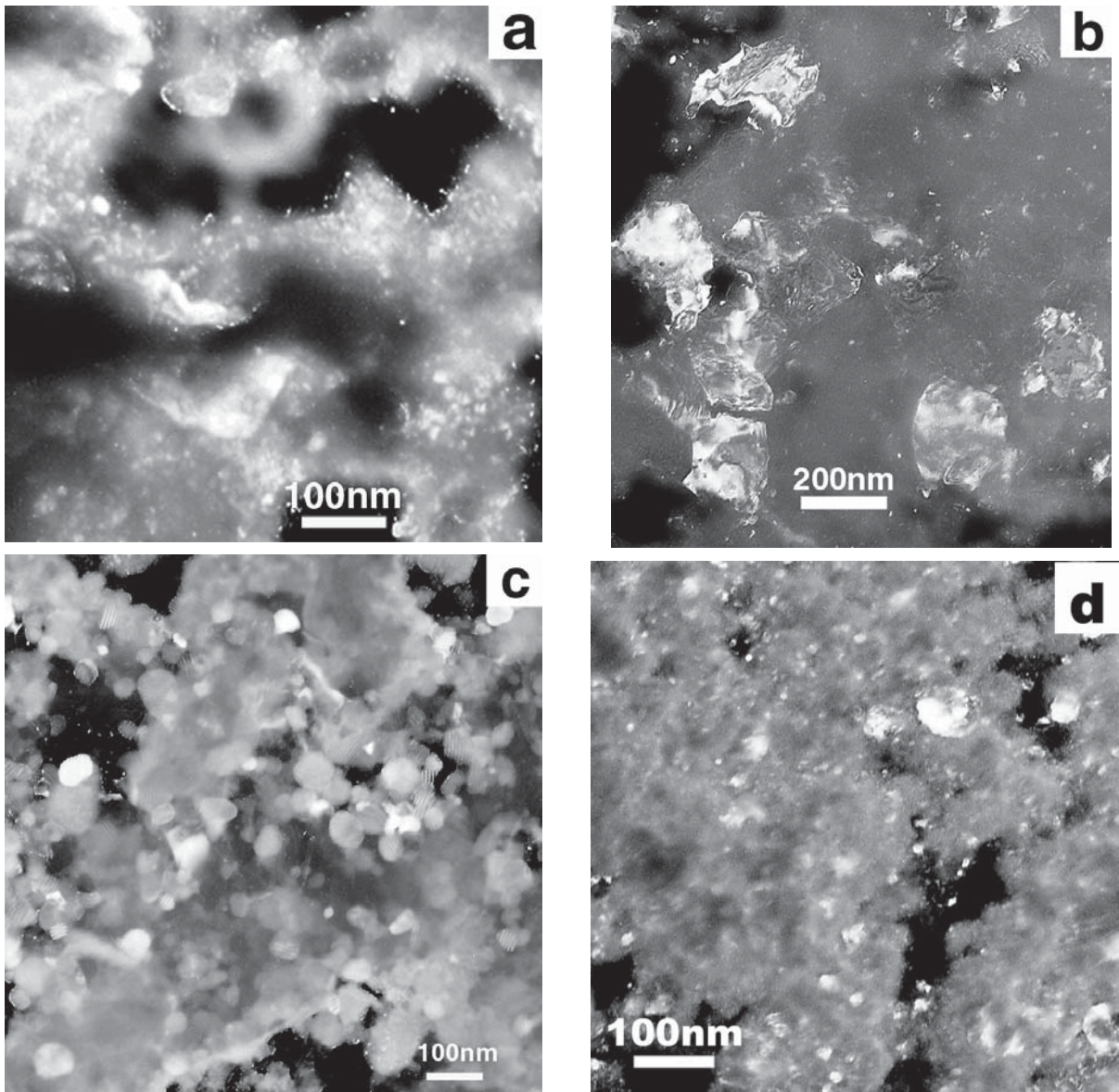


**Fig. 22.** TEM dark field images of Zn ball milled for different times. (a) 1 h (b), 3 h, (c) 18 h, (d) 25 h.

## 6. MECHANICAL PROPERTIES OF *IN SITU* CONSOLIDATED BULK NC Zn

In this section, we will discuss the mechanical properties of bulk nc Zn studied by microhardness, MDBT and uniaxial tensile tests in an attempt to explore the deformation mechanisms in nc Zn.

### 6.1. Strength and ductility of nc Zn studied by microhardness and MDBT tests

The microhardness of BM Zn is plotted vs.  $d^{-1/2}$  in Fig. 24. In general, a linear relationship is observed

with a positive Hall-Petch slope. The hardness of cg Zn [110] falls on the same line with that of BM Zn. Hardness for BM Zn with the smallest grain size, 23 nm, deviates from this linear relation, i.e. it is below the hardness as predicted from the linear relation. The variation of hardness vs.  $d^{-1/2}$  in BM Zn is typical compared to strengthening in many other nc metals, where the hardness of materials is controlled mainly by their average grain size. The hardness of BM Zn is comparable to that of nc Zn obtained from other techniques, such as inert gas condensation [116] and pulsed laser deposition [117]. The hardness of electrodeposited nc Zn, however, is remarkably higher compared with all other studies [13]. This phenomenon, still under investi-

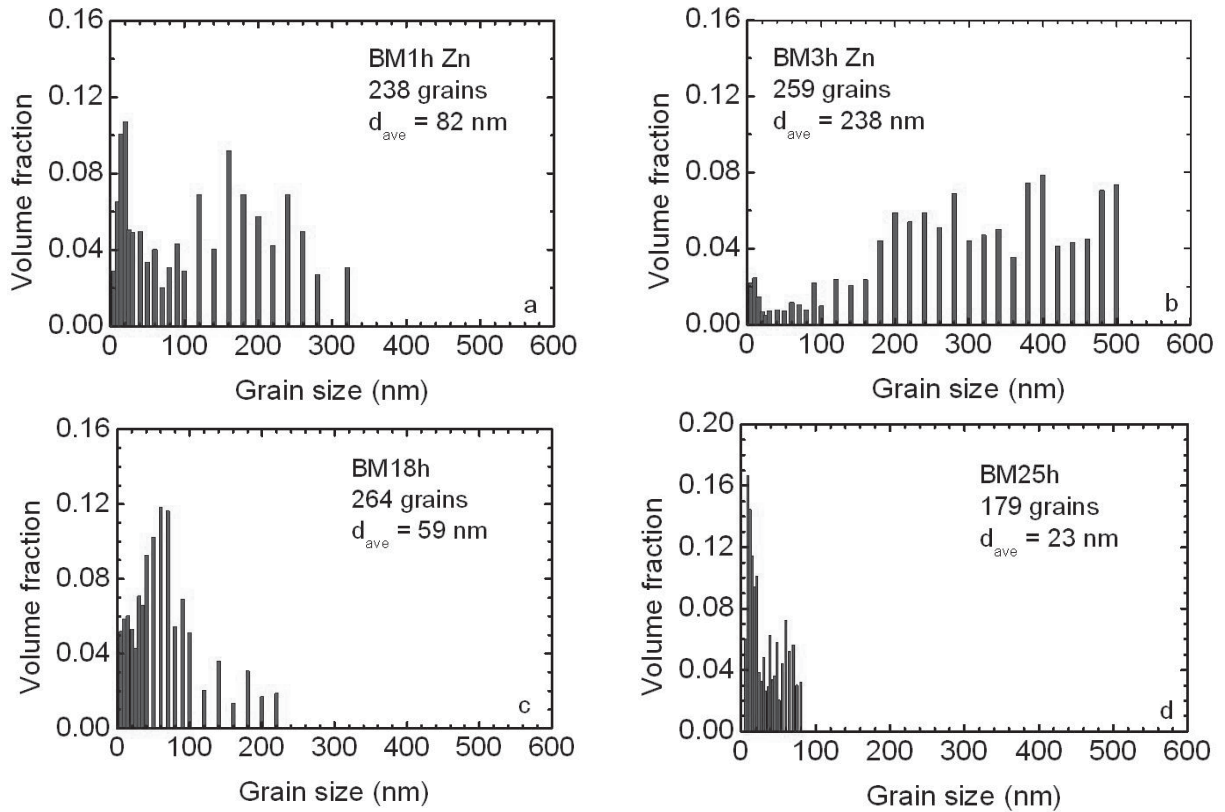


**Fig. 23.** Volume fraction distribution of different grain sizes for Zn milled for different times. (a) BM1h, (b) BM3h, (c) BM18, (d) BM25h.

gation, could be related to the texture of electrodeposited nc Zn [13].

Some of the MDBT results of BM Zn are shown in Fig. 25 in the form of force-displacement curves obtained directly from MDBT tests. Plastic deformation is observed in all the BM Zn samples. The strain calculated from the maximum displacement reached a maximum value of around 5.5% after 3 h of ball milling. The design of the MDBT apparatus required the tests to be stopped at a biaxial tensile strain level of about 5% [107]. Hence the maximum strain observed from MDBT does not represent the real failure strain of the samples. Three times the yield stress,  $3\sigma_y$ , calculated from MDBT is plotted vs. milling time together with hardness results, as shown in Fig. 26. The magnitude and the variation of yield stress with milling time are very consistent with that obtained from microhardness tests. The dramatic drop in hardness/strength between 1 and 3 h at milling is consistent with the large increase in average grain size from 80 nm to 240 nm.

The force-displacement curves can be categorized into five regions (boundaries between region 3, 4 and 5 are not clearly marked for the purpose of

simplicity) for Zn ball milled for less than or equal to 18 h, as shown in Figs. 25a and 25b. The observation of these five regions is typical for ductile materials and is described by Manahan *et al.* [118] as follows:

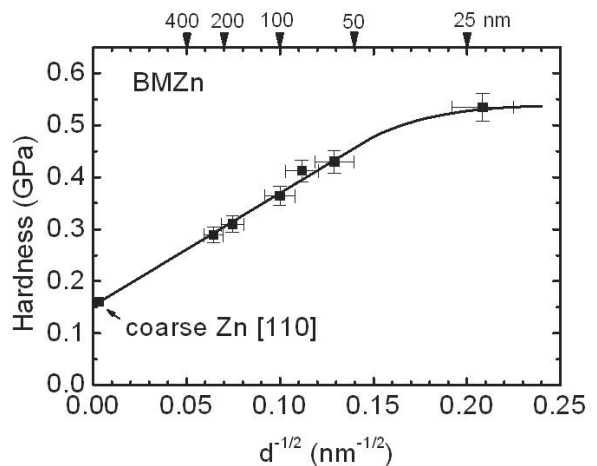


**Fig. 24.** Microhardness vs.  $d^{-1/2}$  for BM Zn and coarse-grained Zn [110].

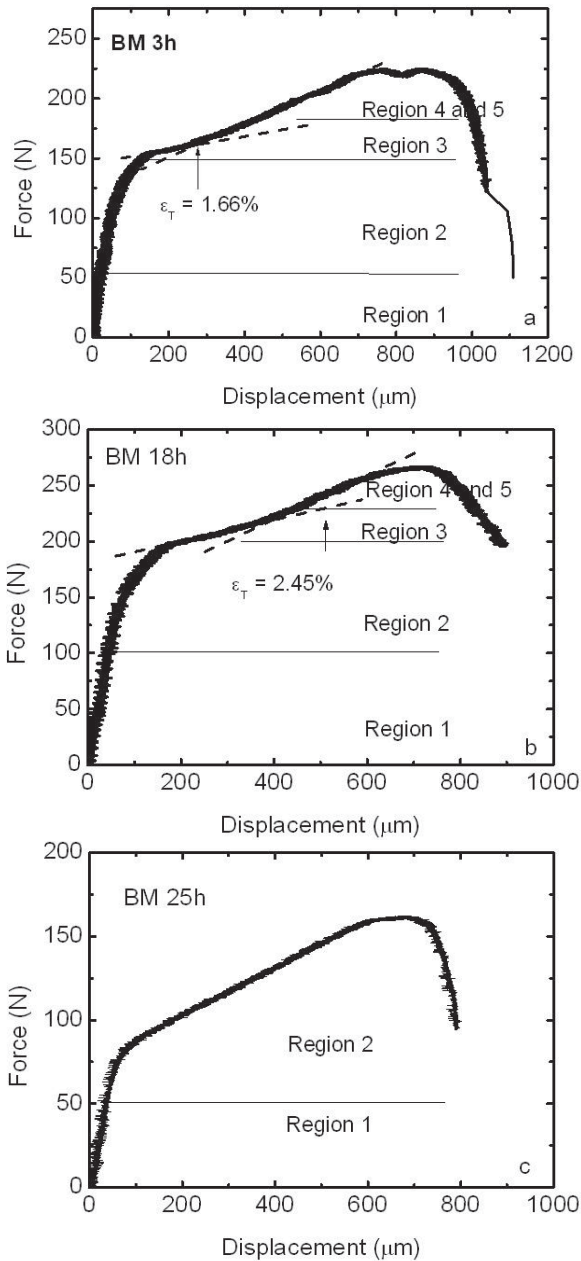


**Fig. 25.** Force vs. displacement calculated from MDBT results for some BM Zn specimens. (a) BM 3h, (b) BM 18h, (c) BM 25h.

Region 1: Elastic deformation governed by Young's modulus, yield stress and the initial hardening rate. Force and displacement has a linear relationship;

Region 2: Departure from linearity due to through thickness and propagation of yield surface from region of contact in the disk radially outward over a large portion of the disk;

Region 3: Transition region indicating that the transition of stress mode from bending to membrane stretching occurs in most regions of the disk;

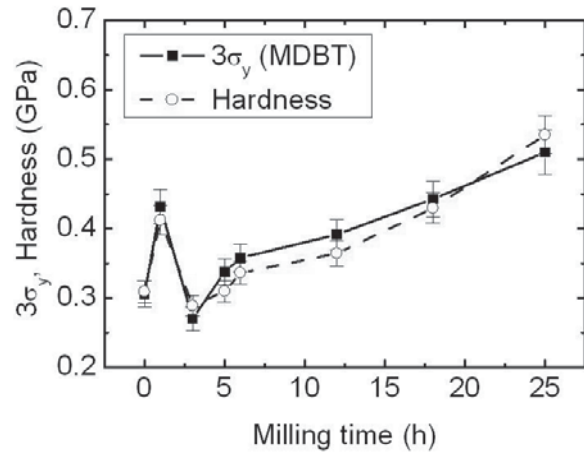


**Fig. 26.** Comparison of  $3\sigma_y$  (result from MDBT) and hardness vs. milling time.

Region 4 and Region 5: Membrane stretching is dominant in most regions of the disk. These stresses eventually lead to fracture in Region 5.

The boundary between the region 1 and region 2 defines the yield stress where the deviation from linearity of force-displacement curves begins. The force was translated into yield stress according to the equation in refs. [119-121]. In the transition region (region 3) for Zn ball milled for  $\leq 18\text{h}$ , the slope of the force-displacement curve is increased by a factor of about 2 after the displacement reaches a certain value. Two tangent dashed lines in Fig. 25a and 25b illustrate the two slopes of the plastic deformation curves. The crossover point of these two tangent lines defines a 'transition strain', which is expressed by  $\epsilon_T$ . This strain,  $\epsilon_T$  is calculated from the displacement at the transition point according to the method used by Huang *et al.* [103]. The strain,  $\epsilon_T$  is roughly at the middle of the transition region (region 3). It is noticed that for BM25h Zn, the transition region (region 3) is not observed, as shown in Fig. 25c. MDBT results of BM1h Zn have a linear elastic region 1 and a small amount of plastic deformation in region 2 before fracture. The variations of transition strain,  $\epsilon_T$  with milling time are shown in Fig. 27. The value of  $\epsilon_T$  shows a steady increase with the increase of milling time. It reaches about 2.4% after 18 h of ball milling. The fact that the transition strain,  $\epsilon_T$  is increased at longer milling time is coincident with the observation that the hardness of BM Zn generally increases with increasing milling time (except the case of BM 1h Zn). A harder, i.e. higher yield stress, sample may lead to a higher  $\epsilon_T$  which is required to transform from bending to the membrane stretching region [122].

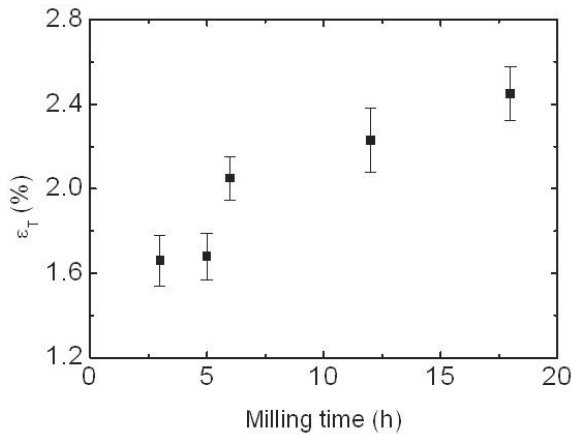


**Fig. 27.** Variation of transition strain ( $\epsilon_T$ ) with milling time for BM Zn.

The surface morphology of BM Zn after MDBT tests is unique. A typical example for BM 18h Zn, studied by scanning electron microscopy, is given in Fig. 28. The specimen, with an average grain size of around 60 nm, has a hat shaped morphology after MDBT. The side view of a BM 18h Zn specimen reveals significant plastic deformation without surface cracks. As mentioned before, MDBT can only detect a maximum strain of about 5% in the materials, whereas the ductility of BM Zn is obviously above the limit of MDBT technique. In the next subsection, we will discuss the ductility and deformation mechanisms in BM Zn studied by uniaxial tensile tests.

## 6.2. Ductility and deformation mechanisms of BM Zn studied by uniaxial tensile tests

Tensile specimens with a 1 mm gage length x 1 mm width were electro discharge machined from Zn disks. Details on the tensile test machine and techniques can be found in references 102 and 123. BM Zn specimens with different grain sizes are all tested. We will first begin with BM3h Zn with an average grain size of 240 nm, focusing on its ductility and deformation mechanisms. We will then compare ductility of BM Zn with different average grain sizes.

**Deformation mechanism in BM3h Zn with an average grain size of 240 nm.** Typical true stress–true strain (called stress–strain hereafter for simplicity) curves at different strain rates are shown in Fig. 29, illustrating a strain rate sensitivity for BM3h Zn. Strain hardening (the increase of stress with

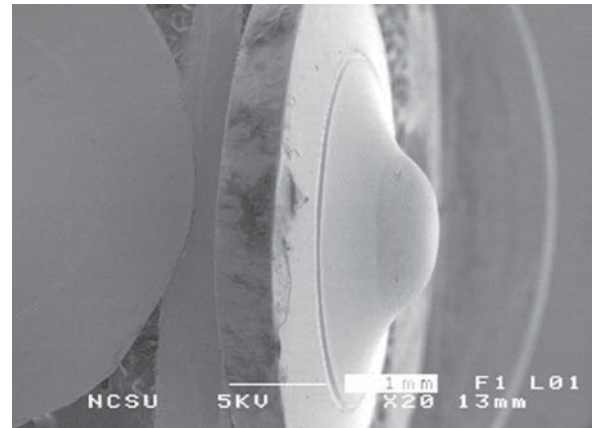


**Fig. 28.** A typical outlook of BM18h Zn specimen after MDBT test.

strain) is observed for a strain rate of  $4 \cdot 10^{-3} \text{ s}^{-1}$  whereas a steady state flow with very little strain hardening was seen at lower strain rates. An elongation of 105% is clearly identified for BM3h Zn tested at the optimum strain rate of  $10^{-3} \text{ s}^{-1}$ , as shown in Fig. 30.

To further explore the strain rate sensitivity of BM3h Zn, jump tests (changing the strain rate by a factor of usually 2 during tensile tests) were performed at 20 °C, 40 °C and 60 °C. Fig. 31 gives two examples of the results. The tensile elongation of BM 3h Zn reached a remarkable value of 110% after the jump test at 20 °C. A typical TEM bright field image in the region near the fracture surface of the BM3h Zn after 110% tensile elongation is shown in Fig. 32, showing equiaxed grains remain despite such large strain. The interior of these equiaxed

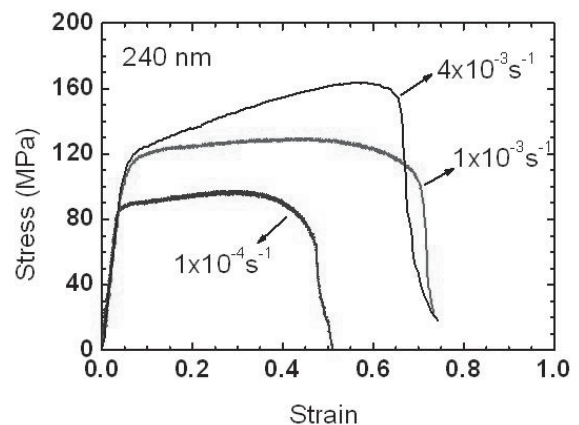


**Fig. 29.** A comparison of tensile tests performed at different strain rate for Zn with 240 nm grain size (BM3h) at room temperature.

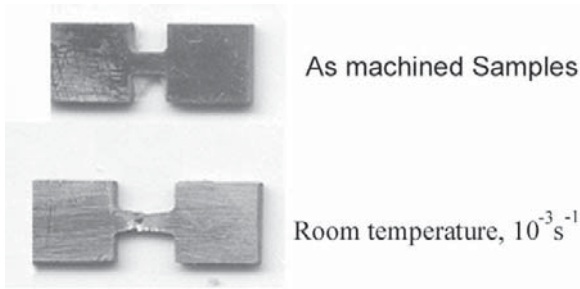


**Fig. 30.** An elongation of 105% is achieved for BM3h Zn tested at room temperature with a strain rate of  $10^{-3} \text{ s}^{-1}$ .

grains has fewer dislocations than were seen in the grains before the tensile test. There are no visible changes in the average grain size before and after tensile tests for all specimens.

At constant strain ( $\epsilon$ ) and temperature ( $T$ ), the strain rate sensitivity,  $m$ , can be calculated according to Eq. (6) given in Sec. 2.3.2. Experimentally, the changes of flow stress as a result of a sudden increase of strain rate are recorded during a jump test. The values of  $m$  are then calculated from the slope in the plot of  $\ln \sigma$  vs.  $\ln \dot{\epsilon}$  as shown in Fig. 33. The  $m$  value is 0.15 for BM3h Zn tested at 20 °C and 40 °C and about 0.17 for Zn tested at 60 °C. High strain rate sensitivity, usually  $m > 0.33$ , is a characteristic of superplastic metals and alloys [84]. Therefore there is basically no superplasticity in ufg Zn tested at room temperature, although a 110% elongation is observed.

A simple assumption for creep is that creep can be considered as a singly activated process which

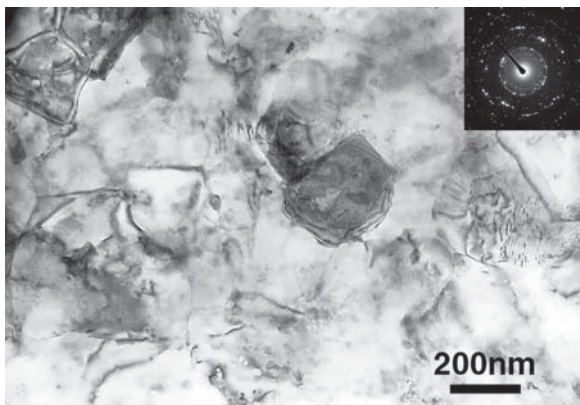


**Fig. 32.** TEM bright field image showing the microstructure of BM3h Zn after the jump tensile test at a temperature of 20 °C.

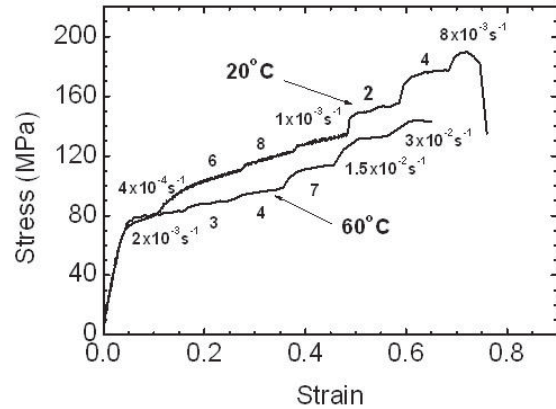


**Fig. 31.** A comparison of jump tests performed on BM3h Zn at 20°C and 60 °C.

can be expressed by an Arrhenius-type rate equation [124]

$$\dot{\epsilon} = A_0 \sigma^n \exp\left(-\frac{Q}{RT}\right), \quad (12)$$

where  $A_0$  is the preexponential complex constant, containing the frequency of vibration of the flow unit, the entropy change and a factor that depends on the structure of the material,  $n$  is the stress exponent,  $Q$  is the activation energy for the rate controlling process, and  $R$  is the universal gas constant, in the units of  $\text{J}\cdot\text{mol}^{-1}\cdot\text{K}^{-1}$ . If we assume a constant  $n$  at different test temperatures and under a constant stress, Eq. (12) can be expressed by

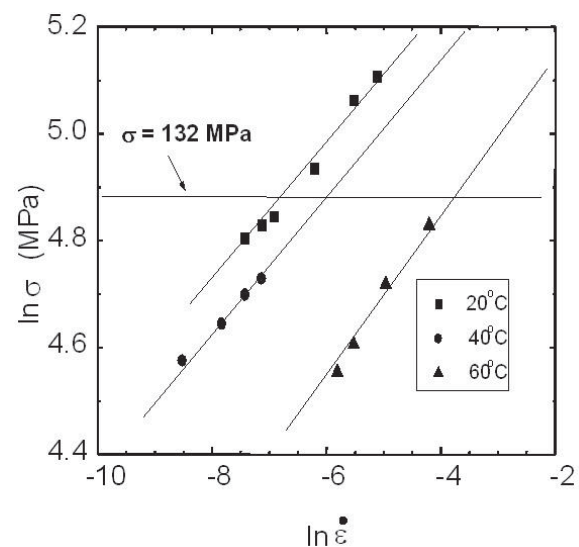


**Fig. 33.** Strain rate dependence of stress obtained from jump tests performed on BM3h Zn at 20 °C, 40 °C and 60 °C respectively.

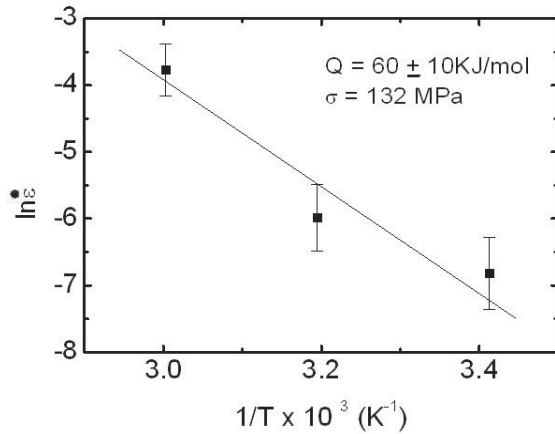


**Fig. 34.** An activation energy of  $Q = 60 \pm 10$  kJ/mol is calculated from the plot of  $\ln \dot{\epsilon}$  vs.  $1/T$  for BM3h Zn.

$$\dot{\epsilon} = A_1 \exp\left(-\frac{Q}{RT}\right), \quad (13)$$

where  $A_1$  is a constant in this case.

By drawing a horizontal line in Fig. 33 at  $\sigma = 132$  MPa, three strain rates are obtained at the cross-over points. In a plot of  $\ln \dot{\epsilon}$  vs.  $1/T$ , Fig. 34,  $Q$  is calculated to be  $60 \pm 10$  kJ/mol. From Eq. (12), the stress exponent,  $n$ , can be obtained as the slope in the plot of  $[\dot{\epsilon} \exp(Q/RT)]$  vs.  $\ln \sigma$ . The value of  $n$  is estimated to be around 6.6 as shown in Fig. 35. The activation energy for plastic deformation in BM3h Zn, around 60 kJ/mol, is very close to the activation energy for grain boundary self diffusion in pure Zn, which is about 59 kJ/mol [98]. The value of stress exponent,  $n = 6.6$ , calculated based on the activation energy is exactly the inverse of strain rate sensitivity ( $m = 0.15$ ), which was calculated initially. An  $n$  value of 6.6 suggests that the deformation mechanism is controlled by dislocation creep. This process could be assisted by grain boundary diffusion. However, dislocation activity in small grains ( $< 50$  nm) is, presumably, very limited, therefore, the dislocation creep mechanism could mainly control the plastic deformation within larger grains. The larger grains ( $> 50$  nm) in BM3h Zn have a volume fraction of greater than 80% [122]. The volume fraction of larger grains kept on decreasing during milling and reduced to around 30% at the longest milling time, 25 h [122].

**Grain size effect on deformation mechanisms and ductility in BM Zn.** Jump tests were also performed on BM5h Zn (with an average grain size of

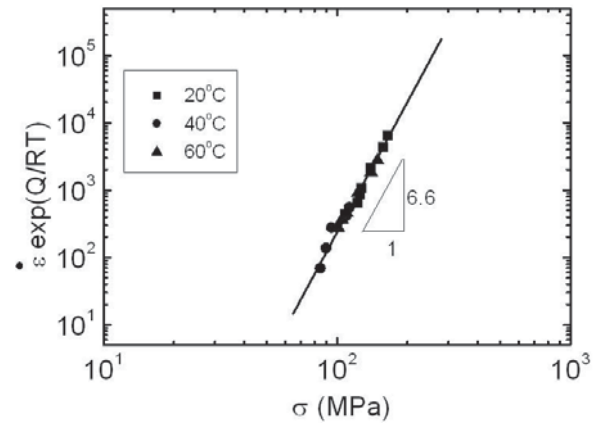


**Fig. 35.** Plot of the normalized strain rate vs. steady state stress over the temperature range of 20–60 °C for BM3h Zn. A stress exponent of  $n = 6.6$  is calculated from this plot.

about 180 nm) to study the strain rate effect on its mechanical properties. An example is shown in Fig. 36a for a jump test performed at 40 °C. A strain of around 60%, which corresponds to an elongation of around 82%, was observed. The  $m$  value is about 0.15 as calculated from Fig. 36b. This  $m$  value is the same as that for BM 3h Zn indicating a similar deformation mechanism, dislocation creep, in the larger grains in both cases.

To study the average grain size effect on mechanical properties, stress-strain curves for Zn with different average grain sizes are plotted together in Fig. 37. The strain rate is  $10^{-3}$  s $^{-1}$  for 238 nm and 59 nm Zn,  $5 \cdot 10^{-3}$  s $^{-1}$  for 178 nm Zn and  $10^{-4}$  s $^{-1}$  for 23 nm Zn. Although the strain rates are a little different from one another, the average grain size effect on mechanical behavior is clear. Yield stress increases, while elongation decreases with the decrease of the average grain size. It should be noted that the magnitude of yield stress calculated from uniaxial tensile tests is very close to that calculated from MDBT studies [122]. The variation of elongation with average grain size is shown in Fig. 38 for UFG and nc Zn as well as Zn with conventional grain sizes (data taken from references 125 and 126). For Zn with conventional grain sizes ( $> 20$   $\mu$ m), elongation increases almost continuously with decreasing grain size. However, for ufg and nc Zn, elongation decreases with the refinement of grain size. The maximum achievable elongation in ufg Zn (BM3h Zn) is about 2–3 times higher than that for cg Zn, while the hardness of ufg Zn is at least a factor of two greater than its cg counterpart.

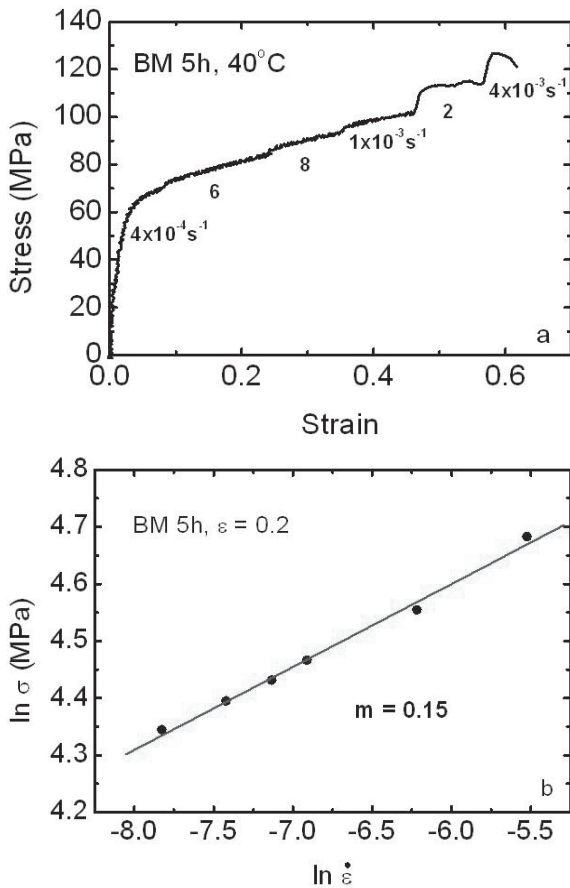


**Fig. 36.** (a) Jump tests performed on BM5h Zn at 40 °C. (b) Strain rate sensitivity of 0.15 is calculated from  $\ln \sigma$  vs.  $\ln \dot{\epsilon}$  plot.

To understand the enhanced ductility in ufg and nc Zn, the following aspects should be considered. First, '*in situ*' consolidation of powder during ball milling is a one-step method compared with the traditional two-step methods (nc powder production + compaction). Bulk Zn specimens all have full density after this one-step technique. Eliminating porosity improved the ductility of these materials. Second, most ufg and/or nc Zn specimens have broad grain size distributions, varying from a few nm to a few hundred nm. Both small grains and large grains may accommodate strain during plastic deformation. However, they may deform in a quite different way. On one hand, the traditional ductile fracture mechanism – nucleation of voids and crack growth by void coalescence – might be avoided or delayed by grain boundary sliding of small grains (5-10 nm). Molecular dynamic simulation of nc Cu and Ni has shown that grain boundary sliding can accommodate a large amount of plastic deformation by inducing viscous sliding of grains with respect to each other without crack or cavity formation [68,127].

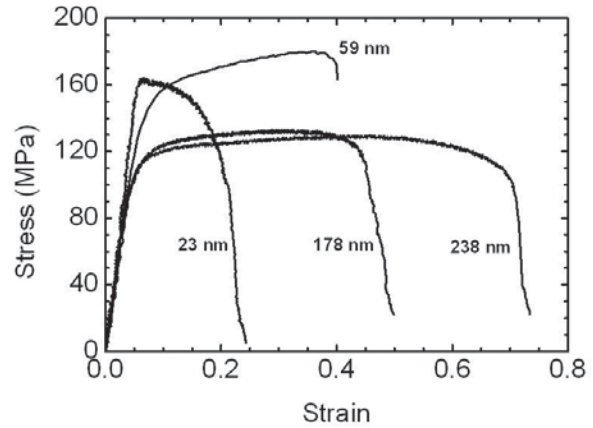


**Fig. 37.** Stress-strain curves for BM3h, BM5h, BM18h and BM25h Zn (with an average grain size of 240 nm, 180 nm, 60 nm and 23 nm respectively) tested at a constant strain rate of  $10^{-4} \text{ s}^{-1}$ - $10^{-3} \text{ s}^{-1}$  at room temperature.

Migrations of the grain boundaries are usually observed during grain boundary sliding events. The fact that grains remain equiaxed after 110% elongation in BM3h Zn is indirect evidence that grain boundary migration is occurring. On the other hand, the stress exponent of  $n = 6.6$  measured from the jump test for BM3h and BM5h Zn suggests a climb controlled dislocation creep deformation mechanism within the larger grains (presumably  $> 50 \text{ nm}$ ) can also accommodate a fraction of the total strain. The superior ductility observed in ufg and nc Zn could therefore be a result of accommodating the strains by a mixture of the two major deformation mechanisms: namely grain

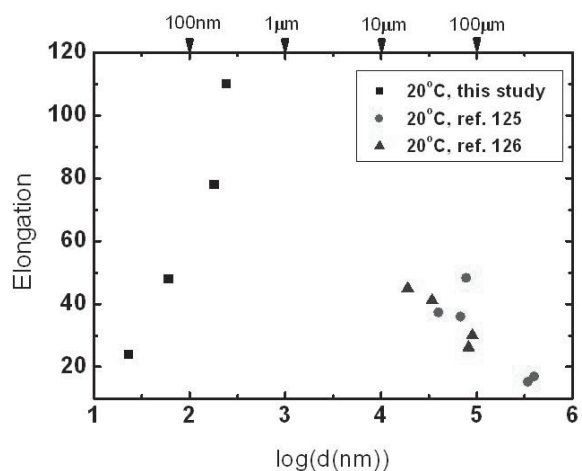


**Fig. 38.** Variation of elongation with average grain size for Zn. BM Zn tested at 20 °C, squares; coarse Zn tested at 20 °C, circles replotted from ref. 125, triangles replotted from ref. 126. All results are obtained under the similar strain rate varied around  $10^{-4} \text{ s}^{-1}$ - $10^{-3} \text{ s}^{-1}$ .

boundary sliding among small nanograins and dislocation creep within the larger grains.

The reduction of elongation with decreasing grain size in ufg and nc Zn is similar to the observation in many other nc elemental metals [53]. Therefore the prediction that ductility will be increased with the decrease of grain size [128] seems to be valid only when the average grain size is beyond a certain limit. During the grain refinement process, the decrease of larger grains will obviously reduce the amount of strains that can be accommodated by them. The increase of small nc grains during refinement, however, should increase the amount of strains accommodated by grain boundary sliding mechanisms. The fact that ductility decreases with the decrease of average grain size could therefore indicate that larger grains possess a higher capacity in accommodating the strain during plastic deformation. Furthermore, BM25h Zn with an average grain size of 23 nm still possesses an elongation of about 20%. This is much larger than values that have been seen in many other nc elemental metals, where only 1-2% elongation is observed [53]. As strain in nc BM25h Zn could be mainly accommodated by grain boundary sliding, the observed ductility, about 20%, in BM25h Zn may indicate an upper limit of ductility for these small nc grains. As shown in Fig. 38, there is, presumably, a maximum elongation somewhere in between the current studies of ufg Zn and those of coarse-grained Zn. A transition of the dependence of ductility on average grain size in Zn may occur in between the two cases.

## 7. COMPARISONS OF THE MICROSTRUCTURE AND MECHANICAL PROPERTIES OF BULK NC Zn PREPARED BY CRYOMILLING AND ROOM TEMPERATURE MILLING

In this section, we will compare the microstructure (sec. 7. 1) and mechanical properties (7. 2) of bulk CM Zn and BM Zn. These two techniques provide different routes to synthesize bulk ufg and/or nc materials. The advantage and disadvantage of each technique are evident after these comparisons. This leads to the idea of optimizing the mechanical properties of bulk ufg and nc Zn by combining the strengths of the two techniques (7. 3).

### 7.1. Grain size and its distributions as a function of temperature

Fig. 39 illustrates the evolution of the average grain sizes with milling time for BM Zn ball milled at room

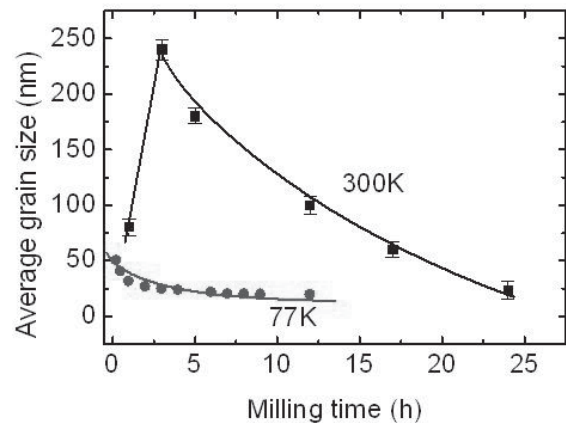


**Fig. 39.** The evolution of the average grain size with milling time for BM Zn milled at room temperature (300K) and CM Zn milled at liquid nitrogen temperature (77K).

temperature (300K) and CM Zn ball milled at 77K. The following differences of microstructure evolution exist for the two techniques. First of all, the average grain size of CM Zn is always smaller than that of BM Zn after the same amount of milling time. Second, the average grain size of CM Zn decreases dramatically to around 50 nm after very short cryomilling time, less than 1 h. The grain size refinement rate is reduced thereafter. Whereas the average grain size of BM Zn decreased significantly to around 80 nm after 1h of ball milling, then it increased to around 240 nm after 3 h of ball milling. The grain refinement rate thereafter is much higher than that of CM Zn during similar milling periods. The value of  $d_{min}$  of Zn could be about 17 nm as evidenced by the saturation of grain size evolution curve in CM Zn. BM Zn may achieve this  $d_{min}$  as well at, however, a much longer milling time. Finally, after comparing the grain size distributions of the two cases Fig. 5 for CM Zn and Fig. 23 for BM Zn, it is clear that CM Zn usually has a narrower grain size distribution than BM Zn milled for the same time.

During the ball milling process, the powder particles undergo a repetitive cold welding and fracture mechanism. Grain size is usually refined faster when fracturing dominates the ball milling process. Dynamic recovery and cold welding are, presumably, significantly reduced by lowering the temperature during milling, such as cryomilling. Thus the grains are refined much faster and they can reach a smaller  $d_{min}$  for CM Zn. The milling temperature effect on grain size refinement is consistent with previous studies on the TiNi intermetallic compound [28]. The grain refinement process in BM Zn could

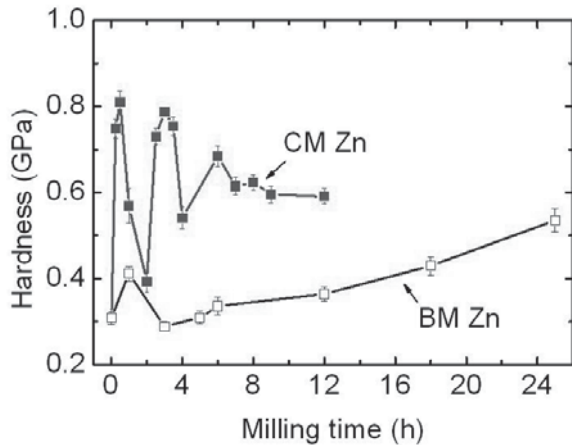


**Fig. 40.** Comparisons of the evolution of microhardness during milling for CM Zn and BM Zn.

be mainly controlled by the Fecht mechanism [16], whereas DRX plays an important role in refining grains during early milling times in CM Zn [17].

## 7.2. Mechanical properties

The evolution of microhardness of CM Zn and BM Zn is compared in Fig. 40. The maximum hardness of CM Zn can reach about 0.8 GPa. At the final stage of cryomilling, the microhardness reaches a saturation value of about 0.6 GPa. The microhardness of BM Zn increases gradually with increasing milling time. A hardness value of about 0.54 GPa is reached after 25h of ball milling, without a clear indication of saturation. The high hardness observed in CM Zn and the hardness evolutions are combinational results of DRX, dislocation density variation and grain size evolutions. Details have been given in Sec. 4.1. The gradual increase of hardness in BM Zn is mainly controlled by its average grain size as detailed in Sec. 6.1. Cryomilling seems to be an efficient method to increase the hardness of Zn by accumulating dislocations more efficiently. However, the ductility of CM Zn is very limited presumably due to the retaining of artifacts during compaction. Whereas BM Zn shows very high ductility varying from 20% for an average grain size of 23 nm to over 100% for an average grain size of 240 nm. At this stage, it is clear that cryomilling has the advantage of refining the grains and therefore increasing the strength in a very short time, while *in situ* consolidation during room temperature milling can produce porosity free bulk materials with high ductility. These comparisons lead to the thought

that high strength and high ductility ufg or nc Zn could be produced by a combination of cryomilling followed by *in situ* consolidation during room temperature milling.

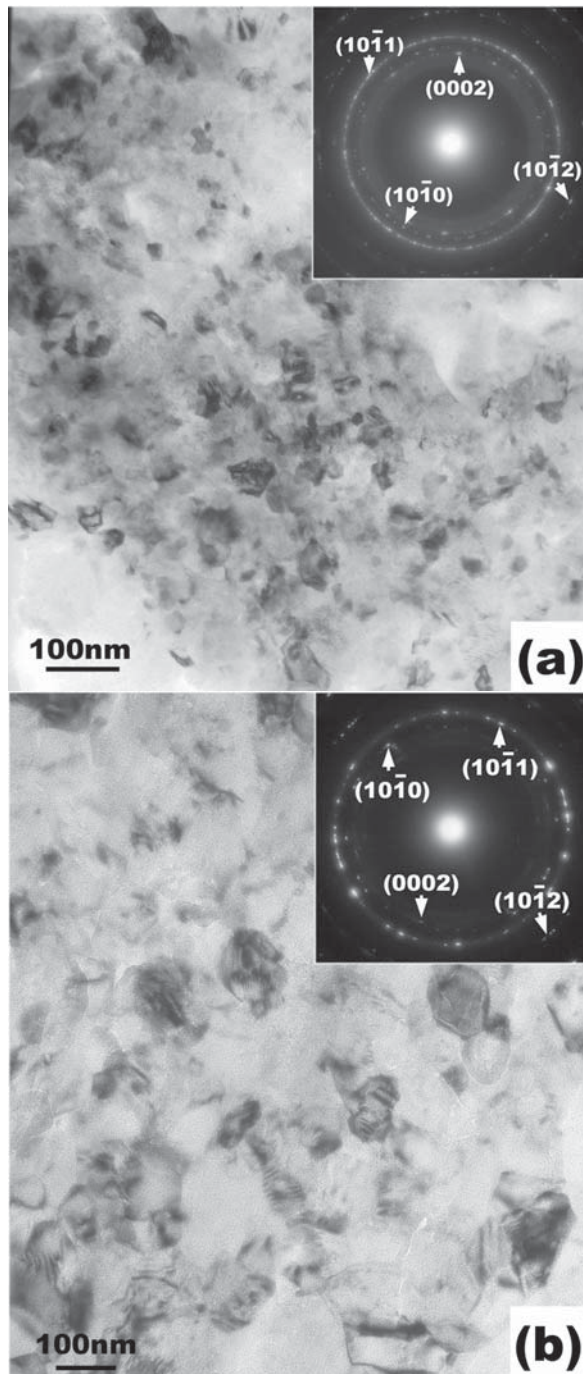
## 7.3. Optimizing mechanical properties of bulk nc Zn by combination of the two techniques

**Microstructural evolution.** Cryomilling was carried out at 77K for times from 0.5 to 3 h in order to synthesize Zn powders with nc microstructures. These powders were then ball milled for 6 h at room temperature. The microstructures of the samples cryomilled and consolidated by room temperature milling were determined by TEM. Examples of the bright field TEM images of samples cryomilled for either 0.5 h or 1 h followed by room temperature milling for 6 h (CM0.5h/BM6h and CM1h/BM6h) are illustrated in Figs. 41a and 41b respectively. The grain size distributions were determined from dark field micrographs. The volume fraction of grains vs. grain size is presented in Fig. 42 for (A) CM0.5h, (a) CM0.5h/BM6h and (B) CM1h, (b) CM1h/BM6h. Similar results were obtained for CM2h/BM6h and CM2h/BM6h Zn. The broad grain size distribution of the cryomilled samples is narrowed by the apparent disappearance of both the very largest and very smallest grains after room temperature milling. As summarized in Table 6, the room temperature ball milling resulted in the average grain sizes for the samples cryomilled for either 0.5 h or 3 h being essentially unchanged, even though the grain size distributions were very different. After room temperature milling, the average grain sizes for the samples cryomilled for 1 and 2 h were approximately doubled. Fewer grains in the range  $< 50$  nm are seen in these samples. However, in all cases the average grain sizes remain below 100 nm after room temperature milling. That is, the microstructure remains nanoscale.

The process of combining cryomilling to provide a nanoscale microstructure with room temperature milling to compact the powders into fully dense spheres has been shown to be successful [129]. The microstructure so developed is significantly finer than can be obtained by simply milling at room temperature for the same time. That is, milling Zn for 6 h at room temperature gives an average grain size of about 150 nm with grains in the distribution over 400 nm in size [122]. The microstructure of CM Zn has been discussed in detail in Sec. 3.1. Briefly speaking, CM0.5h and CM3h Zn have higher dislocation densities, whereas the CM1h and CM2h Zn

**Table 6.** Comparison of average grain size between samples produced by cryomilling (CM) and cryomilling followed by ball milling for 6 h (CM/BM6h).

	Average grain size (nm)	
	CM	CM/BM6h
CM0.5h	37±1	31±3
CM1h	30±1	62±5
CM2h	22±3	68±4
CM3h	23±1	21±2

**Fig. 41.** Bright field TEM micrographs of nc Zn samples. (a) CM0.5h/BM6h, (b) CM1h/BM6h.**Table 7.** Summary of uniaxial tensile test results for samples cryomilled from 0.5 to 3 h and then milled for 6 h at room temperature and BM5h Zn specimen.

Milling time (h)	Yield strength (MPa)	Elongation (%)
CM0.5h/BM6h	140	40
CM1h/BM6h	113	70
CM2h/BM6h	107	75
CM3h/BM6h	160	60
BM5h	101	78

have many small nc grains as a result of DRX. It is likely that the high dislocation densities resulting from cryomilling can be reduced by room temperature recovery processes during milling. The fact that the average grain sizes of the samples cryomilled 1 and 2 h increase after room temperature milling is apparently due to the reduction in the number of the smaller grain sizes to bias the distribution to a larger average value. This may be due to the higher mobility of the newly dynamically recrystallized grains in these samples and therefore the more rapid grain growth kinetics that might result. In fact, in the previous study of modulated hardening behavior [101] it was demonstrated that the grains newly formed by dynamic recrystallization grew rapidly.

**Mechanical properties.** The mechanical properties of the samples ball milled at room temperature were determined by hardness measurements, MDBT measurements for the yield strength, and uniaxial tensile tests. Examples of the stress-strain curves for CM/BM samples are given in Fig. 43 for the samples CM0.5h/BM6h and CM3h/BM6h. Table 7 gives values of the yield strength and fracture strain for all the CM/BM and BM5h Zn specimens. All specimens prepared by the CM/BM technique maintain high strength and considerable ductility. Values of 3 times the yield strength ( $3\sigma_y$ ) and hardness are plotted in Fig. 44 for the samples after cryomilling, open symbols, and after cryomilling followed by room temperature milling, closed symbols. There is reasonable agreement among the  $3\sigma_y$  values determined by the various tests. The strength of the samples consolidated by room temperature milling is significantly reduced from that for the cryomilled condition, although the same trend with cryomilling time is maintained. The reduction of yield

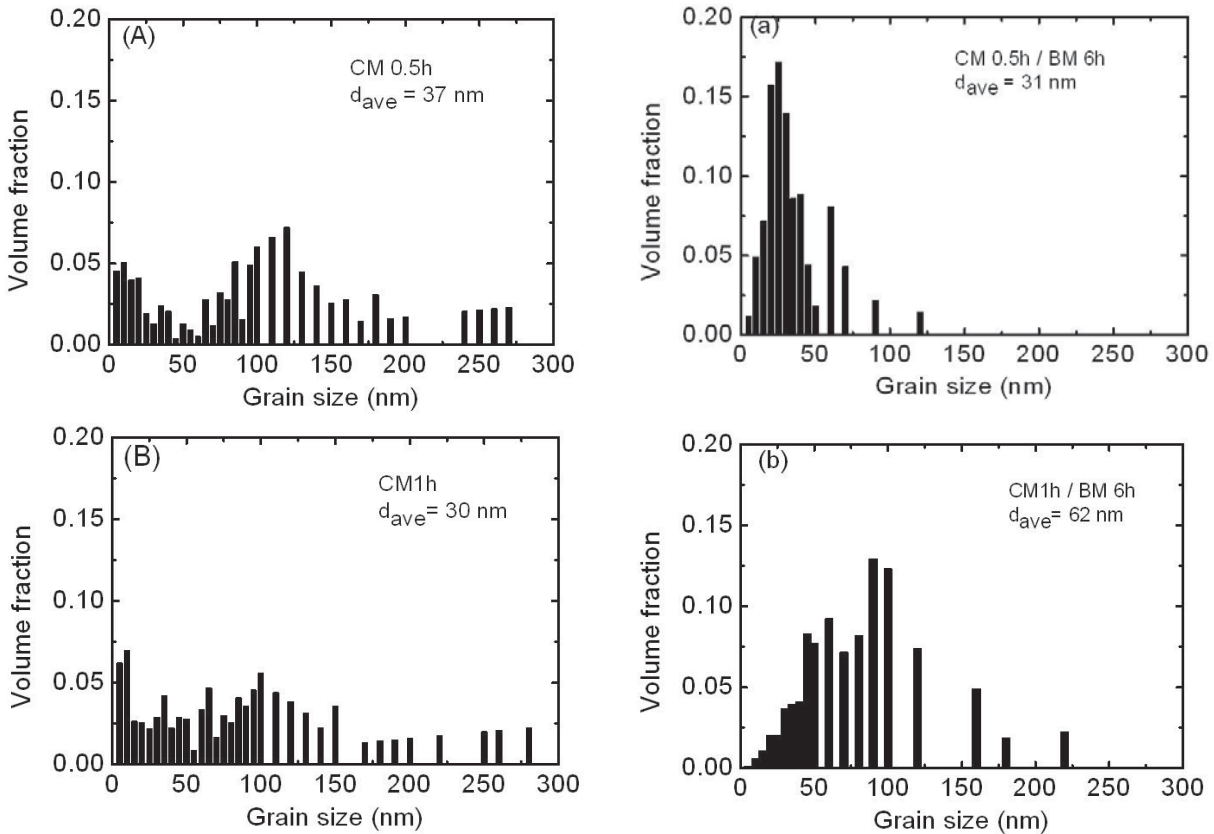


**Fig. 42.** Volume fraction of grains vs. grain size processed at various times via different techniques. (A) CM0.5h, (B) CM1h, (a) CM0.5h/BM6h, (b) CM1h/BM6h.

strength in CM0.5h/BM6h and CM3h/BM6h Zn specimen compared to CM Zn could be a result of decreasing dislocation density due to dynamic recovery. In the case of CM1h/BM6h and CM2h/BM6h Zn, the decreasing strength is consistent with the fact that grain size increases after room temperature ball milling. The CM3h/BM6h Zn specimen has the best combination of strength and ductility. This is in contrast to the results of MDBT estimated ductility which was low for this high strength condition [109]. Thus, the 6h milling at room temperature has modified the microstructure to provide good ductility. The lowering of the dislocation density may be important in this case.

## 8. COMPARISONS OF DEFORMATION MECHANISMS IN BULK UFG AND NC ELEMENTAL METALS

**Effect of grain size and its distribution on yield strength and tensile ductility.** It is clear now that the yield strength of metallic materials can be increased by decreasing their average grain sizes.

The dislocation pile-ups in submicron or larger grains are the main strengthening mechanisms. While the grain size decreases to tens of nm level, dislocation pile-up becomes more and more difficult. At this regime, materials may deform by the single dislocation bowing (Orowan model) mechanism [75,76]. This is typically the case for metallic multilayers

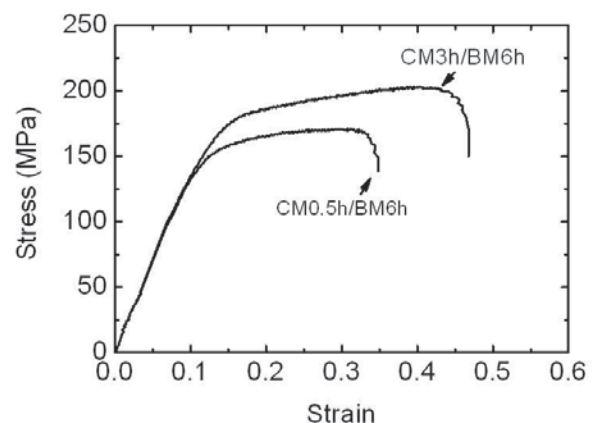


**Fig. 43.** Selected true stress-true strain curves for CM0.5h/BM6h and CM3h/BM6h Zn samples.

**Table 8.** Microstructures and tensile ductility of ufg and nc elemental metals tested at room temperature.

Material	Processing technique	Average grain size (nm)	Grain size distribution	Elongation (%) / strain rate (s <sup>-1</sup> )	Work hardening	Strain rate sensitivity (m)	Reference
Cu	ED		174-251 202-246 273-323	5.1-6.7	Yes		Ebrahimi et al. [56]
Cu	Roll Roll/100°C Roll/425°C	133 152 >1000		36.6	Very little		Ebrahimi et al. [56]
Cu	ECAP ECAP/roll ECAP/roll/ 100°C	300 200 190		15	Yes		Wang et al. [77]
Cu	Roll	200		10	Yes		Wang et al. [77]
Cu	Roll/200°C ECAP	100	200-3000	65 51 (1.0·10 <sup>-3</sup> )		0.09-0.14	Valiev et al. [130]
Cu	Sputter	56 77		17 (8.9·10 <sup>-4</sup> ) 21 (8.9·10 <sup>-4</sup> )			Merz et al. [131]
Ni	ED	6 40		0.7 (4·10 <sup>-4</sup> ) 3.1 (4·10 <sup>-4</sup> )	Yes		Wang et al. [57]
Ni	ED	43-45 38-56 73-79			Yes		Ebrahimi et al. [132]

Table 8. Continued.

Ni	ED	21	13-29	3-4 ( $2.0 \cdot 10^{-4}$ )	Yes	0.01-0.03	Dalla Torre <i>et al.</i> [133]
Ti	ECAP	260		10 ( $1.0-4.0 \cdot 10^{-4}$ )	Very little	0.009	Jia <i>et al.</i> [80]
Ti	HPT	120			Yes		Sergueeva <i>et al.</i> [83]
	HPT/250°C	120			Yes		
	HPT/300°C	150			Yes		
Co	ED	12	8-18	30	Yes		
				6-7 ( $1.0-5.0 \cdot 10^{-4}$ )	Yes		Karimpoor <i>et al.</i> [14]
Zn	<i>in situ</i> consolidation	23 59	5-80 5-320	24 ( $4 \cdot 10^{-4}$ )	n = 0.09-0.2 Very little	N/A	Zhang <i>et al.</i> [34, 122]
		178	5-500	48 ( $4 \cdot 10^{-4}$ )		N/A	
		238	5-500	78 ( $4 \cdot 10^{-4}-8 \cdot 10^{-3}$ ) 110 ( $4 \cdot 10^{-4}-8 \cdot 10^{-3}$ )		0.15	

Note: ED-Electrodeposition, SPD-severe plastic deformation, ECAP-equal channel angular pressing, HPT - high pressure torsion.

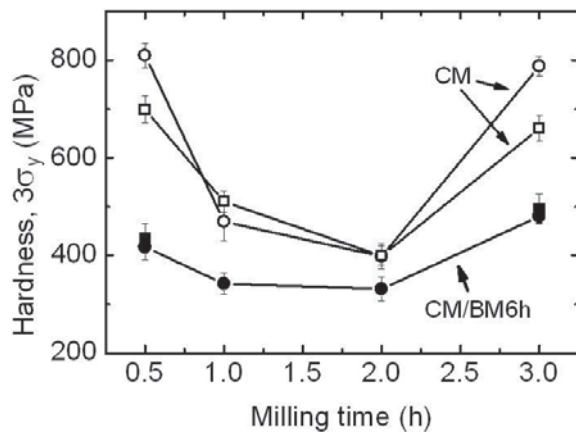


**Fig. 44.** Comparisons of mechanical properties for CM Zn and CM/BM6h Zn as a function of cryomilling time. Open circles, hardness of CMZn; Open squares,  $3\sigma_y$  of CMZn from MDBT; Solid circles,  $3\sigma_y$  of CM/BM6h Zn from uniaxial tensile tests; Solid squares,  $3\sigma_y$  of CM/BM6h Zn from MDBT tests.

with layer thickness on the order of tens of nm. When the grain size becomes very small, a few nm, dislocation activity within the grains becomes less likely and the materials may deform by grain boundary sliding. A broader grain size distribution, especially with an increased volume fraction of coarser grains, tends to significantly reduce the yield stress of the materials [33].

A decrease in ductility is typically observed with the increase of strength when grain sizes are decreased to the nanoscale regime. This phenomenon, a potential hurdle to the application of nc materials has been summarized by Koch *et al.* [53]. Complexity is introduced when comparing tensile test data in the literature for different materials. The following aspects should be considered when comparing these data: (i) the porosity induced by compaction of nc powders usually deteriorates the ductility of nc materials (ii) the starting microstructure of the tested materials could vary greatly in terms of grain size distributions, dislocation densities and textures (iii) tensile ductility is usually lower than compressive ductility (iv) testing conditions may vary, for example strain rate and temperature. Microstructural changes (such as recovery, recrystallization or grain growth) may occur during testing at elevated temperatures.

To make the comparison less complicated, we collect the literature data on ductility with the following characteristics:

- (1) ufg and nc elemental metals without the consideration of alloys
- (2) ufg or nc elemental metals produced by certain processing techniques, where porosity is often not a critical issue, such as severe plastic deformation (rolling, ECAP, high pressure torsion (HPT), *in situ* consolidation), sputtering and electrodeposition.
- (3) ductility data obtained from uniaxial tensile tests at room temperature

As shown in Table 8, the average grain sizes as well as grain size distribution of nc elemental metals are listed. The characteristics of tensile test data, including elongation to failure, strain hardening and strain rate sensitivity are given in the table. Comparisons of strain hardening and strain rate sensitivity will be discussed in the next two subtopics respectively. The temperatures given in the table indicate the annealing temperature before the tensile tests.

Elongation to failure vs. grain size is given in Fig. 45 for different elemental metals. Data on Cu are compared in Fig. 45a. Several things are noticed from this plot: (i) For a specific processing technique, the ductility of Cu decreased with decreasing grain sizes (ii) The ductility of nc Cu is still reasonably high, about 20% elongation for sputtered nc Cu. Strikingly high ductility is observed in ufg Cu produced by ECAP [130] and cold rolling followed by controlled annealing [11]. The enhanced ductility in rolled Cu [11] originated mainly from the accommodation of strain hardening within the larger grains. Although Cu and Ni have similar lattice parameters and the same crystal structure, fcc, the ductility of electrodeposited ufg or nc Ni at room temperature is much lower than that of Cu with similar grain sizes as shown in Fig. 45b. However, ufg or nc Ni tested at elevated temperature possesses superplasticity [86] where abnormal grain growth occurs during tensile tests. It is too early to conclude that ufg or nc Ni possesses poor ductility at room temperature, as there are little tensile test data for ufg or Ni produced by other techniques, such as SPD. Ductility of elemental hcp metals (Ti, Co and Zn) is compared in Fig. 45c. The ductility of Zn and Ti decreases with decreasing average grain sizes. The high ductility in ufg Zn is mainly contributed from the larger grains, a few hundred nm. As the volume fraction of larger Zn grains goes down, the ductility also decreases. Zn and Co with nc grain sizes still retain significant ductility.

These comparisons rule out the effect of porosity on ductility induced by processing techniques.

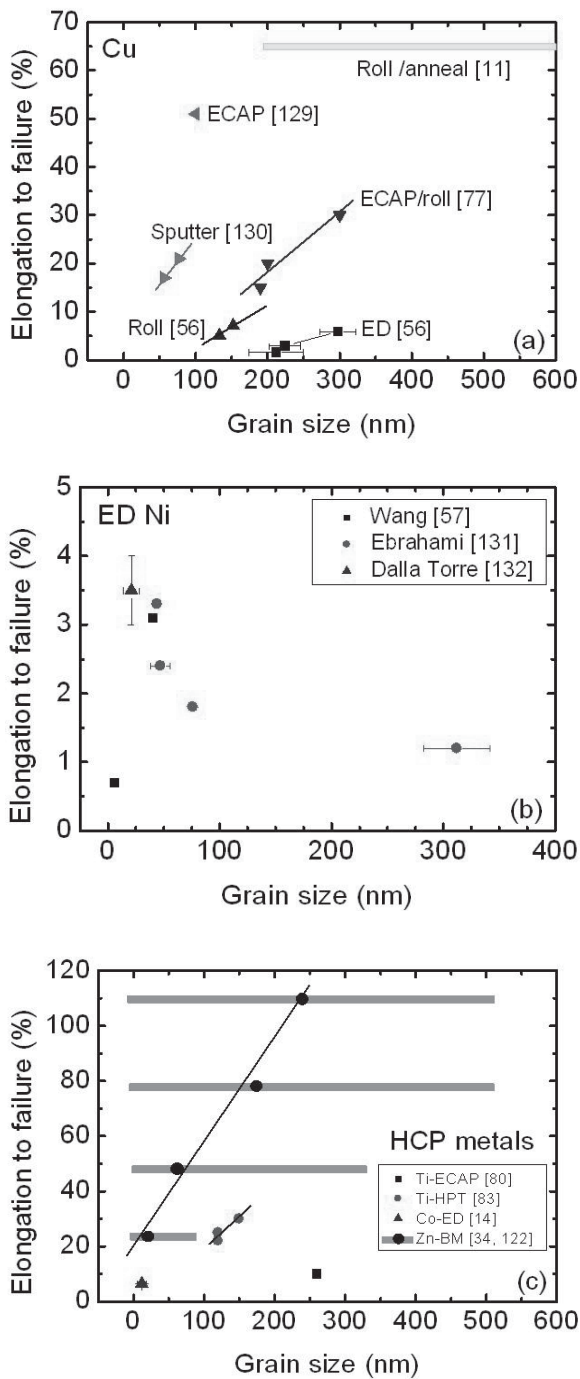


**Fig. 45.** Comparisons of elongation to failure vs. grain size for different elemental metals. (a) Cu (data taken from ref. [11, 56, 77, 130]). The rectangular bars indicate the range of grain sizes for Cu prepared by rolling and annealing [11], the maximum grain size is around 3  $\mu\text{m}$ . (b) electrodeposited Ni (data taken from ref. [57, 131, 132]). The error bars for grain sizes indicate the range of grain sizes. (c) hcp metals, Ti, Co and Zn (data taken from ref. [14, 34, 80, 83, 122]). The rectangular bars stands for the range of grain sizes in Zn, while the black spherical dots on the bars indicate the average grain sizes of the specimens.

Metals with nanoscale grain size possess reasonably good ductility, much higher than previously compared data [53] as a result of improved processing techniques. However, the fact that ductility decreases with decreasing grain size indicates that nanoscale elemental metals may have inherently lower ductility than their microscale counterparts. It is known that dislocation activity is diminishing within nanoscale grains. Strain hardening, important for good ductility, is therefore reduced. In addition the strain that can be accommodated by grain boundary sliding of nanoscale grains is also limited. At higher strains, grain boundary sliding will open up pores and initiate cracks from these pores as demonstrated vividly by Kumar *et al.* [85]. Therefore a composite structure, larger grains embedded in a matrix of small grains, is beneficial in obtaining high strength from the strengthening in the nanoscale matrix and high tensile ductility due to strain hardening in the larger grains. Besides the successful example of highly ductile microscale Cu by Wang *et al.* [11], McFadden *et al.* [86] demonstrated superplasticity in Ni where large grains coexist with nanoscale matrix.

**Strain hardening.** The flow curve of many metals and alloys in the region of uniform plastic deformation can be expressed by power curve relation:

$$\sigma = K\epsilon^n, \quad (14)$$

where  $K$  is the strength coefficient,  $n$  is the strain hardening exponent. By a plot of  $\ln\sigma$  vs.  $\ln\epsilon$ , the  $n$  value can be determined. According to the Considère's criteria for tensile instability,  $d\sigma/d\epsilon < \sigma$ , the value of  $n$  is equal to the true uniform strain [134]. Strain hardening behavior in microscale and nanoscale metals could be very different dependent upon their microstructure prior to tensile deformation. Data in this respect is summarized in Table 8. There are very few studies that provide  $n$  values for microscale and nanoscale metals. In the limited example of electrodeposited nanoscale Co [14], the  $n$  value is lower than that of its coarse-grained counterparts, indicating the uniform strain is smaller in nanoscale metals. This could also be a result of limited strain hardening in small nanoscale grains since strain hardening is important for achieving uniform plastic deformation in materials.

As mentioned in Sec. 2.3.2., research on strain hardening behavior in microscale and nanoscale materials is somewhat controversial. In some cases, microscale and nanoscale materials are found to show strong strain hardening behavior [11, 14, 78, 79], whereas in other cases, they show little strain hardening [80-83]. These controversial observations do not necessarily exclude each other. In fact, they may somehow be consistent with

each other when considering the origins of strain hardening in the materials. Strain hardening in coarse-grained materials comes typically from the accumulation and interaction of dislocations, or interception of slip systems which in turn lead to dislocation jogs or tangles [134]. The flow stress of strain hardened materials is typically proportional to the square root of dislocation density,  $\sigma \propto \rho^{1/2}$ . Strain hardening in ufg or nc metals produced by SPD is usually not significant during tensile tests since these materials are already strain-hardened during processing. However, annealing can usually remove dislocations in these materials and therefore restore their ability to work harden by accumulating more dislocations. If the annealing temperature is chosen such that there is not much increase of average grain size, then high strength and high ductility materials can be produced, such as the cases of ufg Cu [11,82] and Ti [83]. The fact that strain hardening is usually very small in ufg and nc Zn could be an effect of dynamic recovery during tensile tests. Since room temperature is about 40% of the melting temperature for ufg and nc Zn, dynamic recovery could occur during tensile tests and annihilate the dislocations generated by plastic deformation. Strain hardening is observed in ufg Zn tested at higher strain rates, Fig. 29. This evidence may support the fact that dynamic recovery rate can not keep up with the strain hardening rate during higher strain rate tensile tests.

**Strain rate sensitivity.** The plastic instability during a tensile test is quite often related to both strain hardening and strain rate sensitivity. In this case, the plastic instability can be described by Hart's criteria [135]:

$$\gamma + m \leq 1, \quad (15)$$

where  $\gamma$  is a dimensionless strain hardening coefficient,  $\gamma = (1/\sigma)(d\sigma/d\varepsilon)$  and  $m$  is the strain rate sensitivity, defined by Eq. (6) in Sec. 2.3.2. The equation clearly states that both strain hardening and strain-rate hardening contribute to suppressing the onset of plastic instability. Therefore, high strain rate sensitivity may enhance the ductility of materials and is a desirable property.

In the model proposed by Kim *et al.* [136], the strain rate sensitivity for ufg and nc Cu is calculated to increase with decreasing grain size. However, experimentally, the  $m$  values for ufg and nc Cu are usually very low, as shown in Table 8. The  $m$  value is in general very low for ufg and nc materials. It is moderately higher for ufg and nc Zn [34, 123] and much higher for superplastic ufg and nc Ni [86, 137].

It is not clear why strain rate sensitivity is low in many cases, while it is higher in a few other cases.

**Twinning and stacking faults.** The enhanced ductility in ufg Cu is partially attributed to deformation twinning by Wang *et al.* [11]. They believe that twin boundaries can act as barriers to dislocation movement and therefore add extra strain hardening capability into ufg Cu [11]. In fact twin boundaries can be very strong barriers to dislocation crossing and therefore enhance the strength of materials as evidenced and modeled for twinning in sputtered 330 stainless steel films [138,139]. In coarse-grained materials the critical stress to activate slip is usually smaller than that to activation twinning or stacking faults. However, when the grain sizes enter nanoscale regime, the above mentioned phenomena reverse, i.e. twinning is preferred over slip when the grain size is below a certain value, typically tens of nanometers. Deformation twinning can therefore occur in nc metals even with high stacking fault energies [140,141]. The twinning enhanced ductility in ufg and nc metals is therefore based on the enhanced strain hardening due to twin interfaces. The higher ductility observed in nc Cu than that in nc Ni shown in Fig. 45 a and b could be related with the ability to initiate twinning in these materials, as Ni has a much higher stacking fault energy than that in Cu. Sputter deposited nc Cu with a high density of twinning also possesses high tensile ductility [131]. Enhanced ductility in nc Co has been attributed to the high density of stacking faults and twins [14].

In cg materials, ductility enhancement by twinning alone is usually very limited. However, the orientation change resulting from twinning may place new slip systems in a favorable orientation with respect to the stress axis so that additional slip can take place [134]. Furthermore, we speculate that twinning induced orientation change may facilitate the sliding of nanoscale grains and therefore postpone the generation of pores followed by crack initiation as is the case for many nc metals, such as Ni [85,142]. Molecular dynamics simulations as well as *in situ* TEM studies in this respect may help to further explore this possibility.

**Optimizing strength and ductility.** The above discussions have already suggested how to improve the ductility of ufg and nc metals while maintaining their high strength. Basically, enhanced ductility can be achieved by (i) increasing strain hardening (ii) increasing strain rate sensitivity (iii) activating other deformation mechanisms such as twinning or stacking faults (iv) facilitating grain boundary sliding to

postpone the generation of pores along the grain boundaries or triple junctions. As suggested by Ma [143] and Koch [144], a broad grain size distribution may be beneficial to maintain both high strength in the nc matrix and high ductility due to strain hardening in the larger grains. Another way to restore strain hardening ability is to remove dislocations in ufg or nc metals by annealing or recovery. The materials processed in this way may possess lower yield strength, but they can maintain considerable ultimate tensile strength and greatly enhanced ductility. In materials with lower stacking fault energies it is easier to activate enough deformation twinning or stacking faults to maintain some ductility in nc metals. Many issues critical to improve the ductility of ufg and nc metals remain unclear, such as how to improve their strain rate sensitivity and how to avoid or delay the creation of pores by grain boundary sliding during plastic deformation at certain levels of strain.

## SUMMARY

In this article, we attempt to explore the deformation mechanisms in ufg and nc metals by using Zn as an example. The major observations are summarized as follows:

- (1) the evolution of microstructure (grain size and its distribution) in cryomilled nc Zn is controlled by a combination of dynamic recrystallization and the Fecht mechanism.
- (2) the modulated oscillation of hardness during cryomilling is a combinational effect of dynamic recrystallization, average grain size, grain size distribution and dislocation density variations.
- (3) bulk ufg and nc Zn synthesized by *in situ* consolidation during milling possess high tensile ductility and reasonably high strength. The high tensile ductility may have originated from strains accommodated within the larger grains (submicron) and grain boundary sliding of nanoscale grains.
- (4) Several possibilities of improving the tensile ductility of nc metals are described, such as increasing strain hardening and strain rate sensitivity, activating other deformation mechanisms such as twinning or stacking faults and accommodating grain boundary sliding to postpone the generation of pores along the grain boundaries or triple junctions.

## ACKNOWLEDGEMENT

The authors would like to thank Profs. Ronald Scattergood and Jagdish Narayan for helpful discussions. C. C. Koch acknowledges financial support from NSF under grant no. DMR-0201474 and DOE under grant no. DE-FG02-02ER46003. X. Zhang and H. Wang acknowledge support by Director Funded Postdoctoral Fellowship at Los Alamos National Laboratory.

## REFERENCE

- [1] R. Birringer, H. Gleiter, H. P. Klein and P. Marquardt // *Phys. Lett. A*. **102** (1984) 365.
- [2] A. Inoue // *Mater. Sci. Eng.* **A179/A180** (1994) 57.
- [3] R. O. Hughes, S. D. Smith, C. S. Pande, H. R. Johnson and R. W. Armstrong // *Scripta Metall.* **20** (1986) 93.
- [4] K. Lu, W. D. Wei and J. T. Wang // *Scripta Metall. Mater.* **24** (1995) 2319.
- [5] B. H. Kear and P.R. Strutt // *Nano-Structured Mater.* **6** (1995) 227.
- [6] Z. G. Li and D. J. Smith // *Appl. Phys. Lett.* **55** (1989) 919.
- [7] J. Narayan, N. Biunno, R. Singh, O. W. Holland and O. Auciello // *Appl. Phys. Lett.* **51** (1987) 1845.
- [8] C. C. Koch // *Nano-Structured Mater.* **2** (1993) 109.
- [9] R. Z. Valiev, A. V. Korznikov and R. R. Mulyukov // *Mater. Sci. Eng.* **A168** (1993) 141.
- [10] R. Z. Valiev, N. A. Krasilnikov and N. K. Tsenev // *Mater. Sci. Eng.* **A137** (1991) 35.
- [11] Y. Wang, M. Chen, F. Zhou and E. Ma // *Nature* **419** (2002) 912.
- [12] L. Lu, M. L. Sui and K. Lu // *Science* **287** (2000) 1463.
- [13] Kh. Saber, C. C. Koch and P.S. Fedkiw // *Mater. Sci. Eng.* **A341** (2003) 174.
- [14] A. A. Karimpoor, U. Erb, K. T. Aust and G. Palumbo // *Scripta Mater.* **49** (2003) 651.
- [15] A. Misra, M. Verdier, Y. C. Lu, H. Kung, T. E. Mitchell, M. Nastasi and J. D. Embury // *Scripta Mater.* **39** (1998) 555.
- [16] H. J. Fecht // *Nano-Struc. Mater* **6** (1995) 33.
- [17] X. Zhang, H. Wang, J. Narayan and C. C. Koch // *Acta mater.* **49** (2001) 1319.
- [18] Y.M. Wang, M.W. Chen, H.W. Sheng and E. Ma // *J. Mater. Res.* **17** (2002) 3004.
- [19] F. Zhou, X.Z. Liao, Y.T. Zhu, S. Dallek and E.J. Lavernia // *Acta mater.* **51** (2003) 2777.

- [20] J. Eckert, J. C. Holzer, C. E. Krill III and W. L. Johnson // *J. Mater. Res.* **7** (1992) 1751.
- [21] C. C. Koch // *Nano-Struct. Mater.* **9** (1997) 13.
- [22] E. Hellstern, H. J. Fecht, C. Garland and W. L. Johnson // *J. Appl. Phys.* **65** (1989) 305.
- [23] E. Gaffet and M. Harmelin // *J. Less. Comm. Met.* **157** (1990) 201.
- [24] T. D. Shen, C. C. Koch, T. L. McCormick, R. J. Nemanich, J. Y. Huang and J. G. Huang // *J. Mater. Res.* **10** (1995) 139.
- [25] T. D. Shen, W. Q. Ge, K. Y. Wang, M. X. Quan, J. T. Wang, W. D. Wei and C. C. Koch // *Nano-Struct. Mater.* **7** (1996) 393.
- [26] D. Oleszak and P. H. Shingu // *J. Appl. Phys.* **79** (1996) 2975.
- [27] T. G. Nieh and J. Wadsworth // *Scripta Met. et Mater.* **25** (1991) 955.
- [28] K. Yamada and C. C. Koch // *J. Mater. Res.* **8** (1993) 1317.
- [29] C. Suryanarayana // *Prog. Mater. Sci.* **46** (2001) 1.
- [30] J. Eckert, J. C. Holzer and W. L. Johnson // *Scripta Met. et Mater.* **27** (1992) 1105.
- [31] J. Eckert, J. C. Holzer, C. E. Krill and W. L. Johnson // *J. Mater. Res.* **7** (1992) 1980.
- [32] A. I. Salimon, A. M. Korsunsky and A. N. Ivanov // *Mater. Sci. Engg.* **A271** (1999) 196.
- [33] R. Mitra, T. Ungar, T. Morita, P. G. Sanders and J. R. Weertman, In *Advanced Materials for the 21st Century: The 1999 Julia R Weertman Symposium*, ed. by Y.-W. Chung, D. C. Dunand, P. K. Liaw and G. B. Olson (TMS Proceedings, Warrendale, PA, 1999) p. 553.
- [34] X. Zhang, H. Wang, R. O. Scattergood, J. Narayan, C. C. Koch, A. V. Sergueeva and A. K. Mukherjee // *Appl. Phys. Lett.* **81** (2002) 823.
- [35] G. K. Williamson and W. H. Hall // *Acta mater.* **1** (1953) 22.
- [36] B. E. Warren and B. L. Averbach // *J. Appl. Phys.* **21** (1950) 595.
- [37] S. Enzo, M. Sampoli, G. Cocco, L. Schiffrini and L. Battezzati // *Phil. Mag. B* **59** (1989) 169.
- [38] F. J. Humphreys and M. Hatherly, *Recrystallization and Related Annealing Phenomena* (Pergamon Press, 1996).
- [39] G. Masing and J. Raffelsieper // *Z. Metallk.* **41** (1950) 65.
- [40] F. J. Humphreys and J. W. Martin // *Phil. Mag.* **17** (1968) 365.
- [41] M. P. Anderson and R. F. Mehl // *Trans. Metall. Soc. AIME* **161** (1945) 140.
- [42] P. A. Beck and P. R. Sperry // *J. Appl. Phys.* **21** (1950) 150.
- [43] R. K. Ray, W. B. Hutchinson and B. J. Duggan // *Acta Metall.* **23** (1975) 831.
- [44] B. Bay and N. Hansen // *Metall. Trans.* **A10** (1979) 279.
- [45] R. D. Doherty, D. A. Hughes, F. J. Humphreys, J. J. Jonas, D. Juul Jensen, M. E. Kassner, W. E. King, T. R. McNelley, H. J. McQueen and A. D. Rollett // *Mater. Sci. Eng.* **A238** (1997) 219.
- [46] R. Sandström and R. Lagneborg // *Scripta Metall.* **9** (1975) 59.
- [47] W. Roberts and B. Ahlblom // *Acta Metall.* **26** (1978) 801.
- [48] M. D. Drury and F. J. Humphreys // *Acta Metall.* **34** (1986) 2259.
- [49] H. J. McQueen, O. Knustad, N. Ryum and J. K. Solberg // *Scripta Metall.* **19** (1985) 73.
- [50] H. J. McQueen, J. K. Solberg, N. Ryum and E. Nes // *Phil. Mag.* **A60** (1989) 473.
- [51] S. E. Ion, F. J. Humphreys and S. White // *Acta Metall.* **30** (1982) 1909.
- [52] P. G. Sanders, J. A. Eastman and J. R. Weertman // *Acta Mater.* **45** (1997) 4019.
- [53] C. C. Koch, D. G. Morris, K. Lu and A. Inoue // *MRS Bulletin* **24** (1999) 54.
- [54] P. G. Sanders, J. R. Weertman and J. G. Barker // *J. Mater. Res.* **11** (1996) 3110.
- [55] R. Z. Valiev, R. K. Islamgaliev and I. V. Alexandrov // *Prog. Mater. Sci.* **45** (2000) 103.
- [56] F. Ebrahimi, Q. Zhai and D. Kong // *Scripta Mater.* **39** (1998) 315.
- [57] N. Wang, Z. Wang, K. T. Aust and U. Urb // *Mater. Sci. Eng.* **A237** (1997) 150.
- [58] T. D. Shen and R. B. Schwarz // *Appl. Phys. Lett.* **75** (1999) 49.
- [59] T. D. Shen and R. B. Schwarz, submitted for publication.
- [60] G. He, J. Eckert, W. Loeser and L. Schultz // *Nature Mater.* **2** (2003) 33.
- [61] Y. Saito, H. Utsunomiya, N. Tsuji and T. Sakai // *Acta Mater.* **47** (1999) 579.
- [62] M. Atzmon, J. D. Verhoeven, E. D. Gibson and W. L. Johnson // *Appl. Phys. Lett.* **45** (1984) 1052.
- [63] L. Battezzati, P. Pappalepore, F. Durbiano and I. Gallino // *Acta Mater.* **47** (1999) 1901.

- [64] A. Misra, H. Kung, D. Hammon, R. G. Hoagland and M. Nastasi // *Inter. J. Damage Mech.* **12** (2003) 365.
- [65] N. Mara, A. V. Sergueeva, A. K. Mukherjee, In *Creep Deformation: Fundamentals and Applications*, ed. by R. S. Mishra, J. C. Earthman and S. V. Raj, (TMS - Miner. Metals & Mater. Soc., 2002) p.371.
- [66] H. Van Swygenhoven, M. Spaczer, A. Caro and D. Farkas // *Phys. Rev. B* **60** (1999) 22.
- [67] J. Schiötz, T. Vegge, F. D. Di Tolla and K. W. Jacobsen // *Phys. Rev.* **B60** (1999) 11971.
- [68] H. Van Swygenhoven and P. M. Derlet // *Phys. Rev. B* **64** (2001) 224105.
- [69] W. W. Milligan, S. A. Hackney, M. Ke and E. C. Aifantis // *Nanostruct. Mater.* **2** (1993) 267.
- [70] M. Ke, S. A. Hackney, W. W. Milligan and E. C. Aifantis // *Nanostruct. Mater.* **5** (1995) 689.
- [71] J. Chen, W. Wang, L.H. Qian and K. Lu // *Scripta Mater.* **49** (2003) 645.
- [72] D. Feichtinger, P. M. Derlet and H. Van Swygenhoven // *Phys. Rev. B* **67** (2003) 024113.
- [73] J. D. Embury and J. P. Hirth // *Acta Met.* **42** (1994) 2051.
- [74] W. D. Nix // *Mater. Sci. Eng.* **A234-236** (1997) 37.
- [75] A. Misra, M. Verdier, H. Kung, J. D. Embury and J. P. Hirth // *Scripta Mater.* **41** (1999) 973.
- [76] A. Misra, J. P. Hirth and H. Kung // *Phil. Mag. A* **82** (2002) 2935.
- [77] Y. Wang, M. W. Chen and E. Ma // *Appl. Phys. Lett.* **80** (2002) 2395.
- [78] R. Schwaiger, B. Moser, M. Dao, N. Chollacoop and S. Suresh // *Acta Mater.* **51** (2003) 5159.
- [79] L. Lu, L. B. Wang, B. Z. Ding and K. Lu // *J. Mater. Res.* **15** (2000) 270.
- [80] D. Jia, Y. M. Wang, K. T. Ramesh, E. Ma, Y. T. Zhu and R. Z. Valiev // *Appl. Phys. Lett.* **79** (2001) 611.
- [81] S. Hwang, C. Nishimura and P.G. McCormick // *Scripta Mater.* **44** (2001) 1507.
- [82] R. Z. Valiev // *Mater Sci Eng.* **A234-236** (1997) 59.
- [83] A. V. Sergueeva, V. V. Stolyarov, R. Z. Valiev and A. K. Mukherjee // *Scripta Mater.* **45** (2001) 747.
- [84] T. G. Nieh, J. Wadsworth and O. D. Sherby, *Superplasticity in metals and ceramics* (Cambridge University Press, Cambridge, 1997).
- [85] K. S. Kumar, H. Van Swygenhoven and S. Suresh // *Acta Mater.* **51** (2003) 5743.
- [86] S. X. Mcfadden, R. S. Mishra, R. Z. Valiev, A. P. Zhilyaev and A. K. Mukherjee // *Nature* **398** (1999) 684.
- [87] M. Hatherly and A. S. Malin // *Scripta Met. et Mater.* **18** (1984) 449.
- [88] A. A. Ridha and W. B. Hutchinson // *Acta Metall.* **30** (1982) 1929.
- [89] A. S. Malin, M. Hatherly and V. Piegerova, In: *Strength of Metals and Alloys (ICSMA 6). Proceedings of the 6<sup>th</sup> international conference*, ed. by R.C. Gifkins, (Pergamon Press, 1982) Vol. **1**, p. 523.
- [90] G. Gottstein and L. S. Shvindlerman, *Grain Boundary Migration in Metals* (CRC Press. 1999).
- [91] A. S. Nandekar and J. Narayan // *Phil. Mag. A* **61** (1990) 873.
- [92] J. Grewen, In: *Proc. 3<sup>rd</sup> Coll. Eur. Sur Textures* (Pont-a-Mousson, 1973), p. 195.
- [93] X. Zhang, H. Wang, M. Kassem, J. Narayan and C. C. Koch // *J. Mater. Res.* **16** (2001) 3485.
- [94] J. P. Hirth and J. Lothe, *Theory of Dislocations, 2nd Edition*, (New York, Wiley, 1982).
- [95] J. Narayan and A. S. Nandedkar // *Phil. Mag.* **B 63** (1991) 1181.
- [96] J. Schmidt // *Thermochim. Acta* **151** (1989) 333.
- [97] H. E. Kissinger // *Analytic Chemistry* **29** (1957) 1702.
- [98] E. S. Wadja // *Acta Mater.* **2** (1954) 184.
- [99] N. L. Peterson // *J. Nucl. Mater.* **69&70** (1979) 3.
- [100] M. Sluiter and Y. Kawazoe // *Acta Mater.* **47** (1999) 475.
- [101] X. Zhang, H. Wang, R.O. Scattergood, J. Narayan and C.C. Koch // *Acta Mater.* **50** (2002) 3995.
- [102] X. Zhang, *Ph.D. Dissertation, North Carolina State University*, 2001.
- [103] F. M. Huang, M. L. Hamilton and G. L. Wire // *Nucl. Techn.* **57** (1982) 234.
- [104] M. P. Manahan, A. S. Argon and O. K. Harling // *J. Nucl. Mater.* **103&104** (1981) 1545.
- [105] G. E. Lucas // *Metall. Trans.* **21A** (1990) 1105.
- [106] D. E. Meyers, F. C. Chen, J. Zhang and A. J. Ardell // *J. Test. Eval.* **21** (1993) 263.

- [107] V. Y. Gertsman, M. Hoffmann, H. Gleiter and R. Birringer // *Acta Metall. Mater.* **42** (1994) 3539.
- [108] T. R. Malow and C. C. Koch // *Acta Mater.* **46** (1998) 6459.
- [109] X. Zhang, H. Wang, R.O. Scattergood, J. Narayan and C.C. Koch // *Acta Mater.* **50** (2002) 3527.
- [110] *Metals Handbook, Desk Edition* (ASM, Metals Park, OH, 1985).
- [111] H. Luthy, R. A. White and O. D. Sherby // *Mater. Sci. Eng.* **39** (1979) 211.
- [112] O. D. Sherby and J. Wadsworth // *Prog. Mater. Sci.* **33** (1989) 169.
- [113] X. Zhang, H. Wang, M. Kassem, J. Narayan and C. C. Koch // *Scripta Mater.* **46** (2002) 661.
- [114] J. Y. Huang, Y. K. Wu and H. Q. Ye // *Mater. Sci. Eng.* **A199** (1995) 165.
- [115] A. M. Harris, G. B. Schaffer and N. W. Page, In: *Proc. 2<sup>nd</sup> Conference on Structural Applications of Mechanical Alloying* (ASM International, Vancouver, British Columbia, Canada, 1993) p. 20.
- [116] Q. Xia, C.H. Hamilton, K. Recknagle, C.T. Crowe and G.S. Collins // *Mater. Sci. Forum* **170-172** (1994) 147.
- [117] J. Narayan // *J. Nanoparticle Res.* **2** (2000) 91.
- [118] M. P. Manahan, A. E. Browning, A. S. Argon and O. K. Harling, In: *The Use of Small-Scale Specimens for Testing Irradiated Material*, ed. by W. R. Corwin and G. E. Lucas (ASTM STP 888, Philadelphia, 1986) p.17.
- [119] W. C. Young, *Roark's Formulas for Stress and Strain, 5<sup>th</sup> ed.* (Mc Graw-Hill, New York, NY, 1989).
- [120] M. N. Giovan and G. J. Sines // *Amer. Ceram. Soc.* **62** (1979) 510.
- [121] M. Hoffmann and R. Birringer // *Mater. Sci. Eng.* **A202** (1995) 18.
- [122] X. Zhang, H. Wang, R. O. Scattergood, J. Narayan and C. C. Koch // *Mater. Sci. Eng.* **A344** (2003) 175.
- [123] X. Zhang, H. Wang, R. O. Scattergood, J. Narayan, A.V. Sergueeva, A.K. Mukherjee and C. C. Koch // *Acta Mater.* **50** (2002) 4823.
- [124] A. K. Mukherjee, J. E. Bird and J. E. Dorn // *Trans. Am. Soc. Metals* **62** (1969) 155.
- [125] F. Chmelik, Z. Trojanova, P. Lukac and Z. Prevorovsky // *J. Mater. Sci. Lett.* **12** (1993) 1166.
- [126] K. R. Rao, S. Ranganathan and D. H. Sastry // *Bull. Mater. Sci.* **8** (1986) 81.
- [127] J. Schiotz, F. D. Di Tolla and K. W. Jacobsen // *Nature* **391** (1998) 561.
- [128] R. Bohn, T. Haubold, R. Birringer and H. Gleiter // *Scripta Metall. Mater.* **25** (1991) 811.
- [129] X. K. Zhu, X. Zhang, H. Wang, A. V. Sergueeva, A. K. Mukherjee, R. O. Scattergood, J. Narayan and C. C. Koch // *Scripta Mater.* **49** (2003) 429
- [130] R. Z. Valiev, I. V. Alexandrov, Y. T. Zhu and T. C. Lowe // *J. Mater. Res.* **17** (2002) 5.
- [131] M. D. Merz and S. D. Dahlgren // *J. Appl. Phys.* **46** (1975) 3235.
- [132] F. Ebrahimi, G. R. Bourne, M. S. Kelly and T. E. Matthews // *Nanostruc. Mater.* **11** (1999) 343.
- [133] F. Dalla Torre, H. Van Swygenhoven and M. Victoria // *Acta Mater.* **50** (2002) 3957.
- [134] G. E. Dieter, *Mechanical Metallurgy, 3<sup>rd</sup>, Ed.* (McGraw Hill, Boston, 1986).
- [135] E. W. Hart // *Acta Metall.* **15** (1967) 351.
- [136] H. S. Kim and Y. Estrin // *Appl. Phys. Lett.* **79** (2001) 4115.
- [137] S. X. McFadden, A. P. Zhilyaev, R. S. Mishra and A. K. Mukherjee // *Mater. Lett.* **45** (2000) 345.
- [138] X. Zhang, A. Misra, H. Wang, T. D. Shen, M. Nastasi, T. E. Mitchell, J. P. Hirth, R. G. Hoagland and J. D. Embury // *Acta Mater.* **52** (2004) 995.
- [139] X. Zhang, A. Misra, H. Wang, M. Nastasi, J. D. Embury, T. E. Mitchell, R. G. Hoagland and J. P. Hirth // *Appl. Phys. Lett.* **84** (2004) 1096.
- [140] M. Chen, E. Ma, K. J. Hemker, H. Sheng, Y. Wang and X. Cheng // *Science* **300** (2003) 1275.
- [141] X. Z. Liao, Y. H. Zhao, S. G. Srinivasan, Y. T. Zhu, R. Z. Valiev and D. V. Gunterov // *Appl. Phys. Lett.* **84** (2004) 592.
- [142] K. S. Kumar, S. Suresh, M. F. Chisholm, J. A. Horton and P. Wang // *Acta Mater.* **51** (2003) 387.
- [143] E. Ma // *Scripta Mater.* **49** (2003) 663.
- [144] C. C. Koch // *Scripta Mater.* **49** (2003) 657.